BBA - Bioenergetics 1860 (2019) 659–678

Contents lists available at ScienceDirect

BBA - Bioenergetics

journal homepage: www.elsevier.com/locate/bbabio

Mitochondrial cristae narrowing upon higher 2-oxoglutarate load

Andrea Dlasková[a,1], Tomáš Špaček[a,1], Hana Engstová[a,1], Jitka Špačková[a], Adam Schröfel[b], Blanka Holendová[a], Katarína Smolková[a], Lydie Plecitá-Hlavatá[a], Petr Ježek[a,*]

[a] Department of Mitochondrial Physiology, No. 75, Institute of Physiology, , Czech Academy of Sciences, Prague, Czech Republic
[b] Imaging Methods Core Facility, BIOCEV, Faculty of Sciences, Charles University, 242 50 Vestec, Czech Republic

ARTICLE INFO

Keywords:
Mitochondrial cristae
Hypoxia
Dimethyl-2-oxoglutarate
3D super-resolution microscopy
Direct stochastic optical reconstruction microscopy
dSTORM
Mic60/mitofilin
ATP-synthase dimers

ABSTRACT

Hypoxia causes mitochondrial cristae widening, enabled by the ~20% degradation of Mic60/mitofilin, with concomitant clustering of the MICOS complex, reflecting the widening of crista junctions (outlets) (Plecitá-Hlavatá et al. FASEB J., 2016 30:1941–1957). Attempting to accelerate metabolism by the addition of membrane-permeant dimethyl-2-oxoglutarate (dm2OG) to HepG2 cells *pre*-adapted to hypoxia, we found cristae narrowing by transmission electron microscopy. Glycolytic HepG2 cells, which downregulate hypoxic respiration, instantly increased respiration with dm2OG. Changes in intracristal space (ICS) morphology were also revealed by 3D super-resolution microscopy using Eos-conjugated ICS-located lactamase-β. Cristae topology was resolved in detail by focused-ion beam/scanning electron microscopy (FIB/SEM). The spatial relocations of key cristae-shaping proteins were indicated by immunocytochemical stochastic 3D super-resolution microscopy (dSTORM), while analyzing inter-antibody-distance histograms: *i*) ATP-synthase dimers exhibited a higher fraction of shorter inter-distances between bound F_1-α primary Alexa-Fluor-647-conjugated antibodies, indicating cristae narrowing. *ii*) Mic60/mitofilin clusters (established upon hypoxia) decayed, restoring isotropic random Mic60/mitofilin distribution (a signature of normoxia). *iii*) outer membrane SAMM50 formed more focused clusters. Less abundant fractions of higher ATP-synthase oligomers of hypoxic samples on blue-native electrophoresis became more abundant fractions at the high dm2OG load and at normoxia. This indicates more labile ATP-synthase dimeric rows established at crista rims upon hypoxia, strengthened at normoxia or dm2OG-substrate load. Hypothetically, the increased Krebs substrate load stimulates the cross-linking/strengthening of rows of ATP-synthase dimers at the crista rims, making them sharper. Crista narrowing ensures a more efficient coupling of proton pumping to ATP synthesis. We demonstrated that cristae morphology changes even within minutes.

1. Introduction

Cristae morphology may reflect the energetic demands of the cell [1–5]. The architecture of mitochondrial cristae has been resolved in isolated mitochondria [6]. Cristae morphology is controlled by cristae-shaping proteins [6]. The “mitochondrial contact site and cristae organizing system” (MICOS) complex exists at crista junctions with the outer mitochondrial membrane (OMM) [8–12]. MICOS joins the OMM translocase of the outer membrane β-barrel proteins (TOB)/sorting and assembly machinery (SAM) complex [13,14]. The SAM/TOB complex contains the SAMM50 protein bearing a polypeptide transport-associated (POTRA) domain, which binds the Mitofilin/Mic60 subunit of MICOS [13]. MICOS is a dynamic system, containing numerous Mic subunits denoted by their molecular mass [15]. Notably, the oligomers of Mic10 subunits bend the inner mitochondrial membrane (IMM) at crista junctions [16,17]. Various isoforms and heteromers of optic athrophy-1 protein (OPA1) guard the crista outlets under crista junctions with OMM [18–22]. These outlets form hollow connections with the peripheral intermembrane space. The latter forms a tubular sandwich with the OMM and the inner boundary membrane (IBM), a non-invaginated portion of the IMM. Several other components act in the vicinity of crista outlets, such as ROMO1 and prohibitins [2,7].

Cristae are determined by the highly invaginated IMM. Cristae are typically perpendicular or tilted to the longitudinal axis of mitochondrial network tubules. The cristae membranes thus form prolonged “sacks” encompassing a lumen, termed the intracristal space (ICS). A

* Corresponding author at: Department No. 75, Institute of Physiology, Academy of Sciences of the Czech Republic, Vídeňská 1083, 14220 Prague 4, Czech Republic.
E-mail address: jezek@biomed.cas.cz (P. Ježek).
[1] These authors contributed equally.

https://doi.org/10.1016/j.bbabio.2019.06.015
Received 29 January 2019; Received in revised form 19 June 2019; Accepted 21 June 2019
Available online 25 June 2019

single crista lamella may even have more than one crista outlet to the IBM, hence such a crista can appear to be branched in certain sections acquired with transmission electron microscopy (TEM). In the TEM images of sections of the matrix (crista lumen), cristae appear as typical "textbook" black & white strips of mitochondria. These strips represent the shortest dimension *w* of the 3D crista, the lamellar topology of which could instead be approximated by a prolonged cuboid. Note also, in reality, the apparently individual mitochondria in TEM images reflect sections of the continuous mitochondrial network, apparent in numerous cell types.

The sharpness of cristae edge is determined by the rows of the ATP-synthase dimers [23–28]. It has been hypothesized that the ATP-synthase dimers in these rows form sharp cristae rims, since the ATP-synthase dimeric structure is able to bend the lipid bilayer [25,28]. These rims might be stabilized by certain small proteins. Hypothetically, the neighbor dimers of the ATP-synthase may even be "cross-linked" along the longitudinal cristae rim axis by such small proteins or their oligomers. Sir John Walker's group suggested DAPIT to be such a "cross-linker" [29], despite the fact that each odd ATP-synthase dimer should be turned 180° to ensure the interaction of the asymmetrically bound DAPIT. DAPIT is an ortholog of yeast ATP-synthase subunit ***k***, also termed *Usmg*5 in the rat genome (up-regulated during skeletal muscle growth 5) [30–34]. Speculations could be made that the DAPIT upregulation alone [26] might predetermine rich and longer cristae upon skeletal muscle growth.

Moreover, a side function has been proposed for Mic10, the smallest MICOS component, which is most likely provided by Mic10 oligomers. The canonical function of Mic10 lies in the ability of oligomeric Mic10 to form a curvature of crista outlets [16,17,35]. While interacting with the ATP-synthase stator subunit ***e*** [36,37], Mic10 might also cross-link and stabilize the neighbor ATP-synthase dimers quite simply, due to the central location of the subunit ***e*** [29]. Thus Mic10 oligomers might also hypothetically stabilize the ATP-synthase rows and contribute to the establishment of sharp rims of the ICS lipid bilayer. Nevertheless, it must be determined whether a pool of the ATP-synthase bound Mic10 exists only in the vicinity of the crista junctions or along the whole length of the cristae.

The cristae morphology reportedly changed due to the IMM-potential- ($\Delta\Psi$-) sensitivity of OPA1 cleavage [7] or upon PTEN-induced putative kinase-1- (PINK1-) mediated protein degradation, in conjunction with Parkin and the ubiquitin-proteasome system [38]. Cristae widening has been also linked to mitofilin/Mic60 and OPA1 down-regulation during placental trophoblast differentiation into syncytiotrophoblasts, which maintains progesterone production [39].

The detailed morphology of cristae is best acquired using FIB/SEM tomography or cryo-electron tomography [23–27]. 3D fluorescence super-resolution microscopy was rarely able to resolve cristae [40]. The purely physical method stimulated emission depletion (STED) microscopy and stochastic types of microscopy (relying on algorithms for localization) can estimate some features, due to their ability to identify proteins [41–43]. This is done either by overexpression of fluorescent protein-conjugates or the insertion of tags into the studied proteins (fluorescently labeled prior to measurements) or using fluorescent antibodies [41]. For stochastic techniques, such as direct stochastic optical reconstruction microscopy (dSTORM), it is best to use the fluorescent primary antibodies or so-called nanobodies, so as not to harm the resolution [41]. During the dSTORM acquisition of fixed samples, stochastic blinking of the fluorophore attached on the antibody is recorded and knowledge of the point-spread function then serves to localize the particular point using the proper algorithm [41–43]. In our 3D biplane set-up, the resolution along the z-axis is achieved by recording the asymmetrical position of the point spread function between the two planes focused by a camera [42,43]. Despite the inability of 3D dSTORM to resolve cristae, the analyses of inter-distances between the localized antibodies can provide certain information [43].

We have previously reported a remarkable cristae widening [1] related to the hypoxic adaptation of hepatocellular carcinoma HepG2 cells [44,45]. Cristae widening and ICS inflation occurred due to a partial 20% downregulation of mitofilin/Mic60 with the concomitant detachment of MICOS from the OMM [1]. Moreover, the cristae widening with simultaneous shortening of their lengths correlated with apparently less ATP-synthase dimers, immunodetected on the blue-native polyacrylamide electrophoresis gels (BN-PAGE) of solubilized mitochondria isolated from hypoxic cells [1]. Now, we hypothesize that this reflects the more labile ATP-synthase dimeric rows existing in vivo in hypoxic cells. In contrast, when the BN-PAGE of solubilized mitochondria from normoxic cells reveals more dimers, and even tetramers and hexamers as the remnants of dimeric rows, this should reflect a higher in vivo stabilization of these ATP-synthase dimeric rows. We can speculate that a higher fraction of the recruited small proteins, such as DAPIT and Mic10, stabilizes the rows of ATP-synthase dimers, which subsequently form a sharper edge of the crista, and consequently a smaller ICS volume. Such a reduced ICS volume could lead to increased OXPHOS efficiency [2].

We have suggested that physiological hypoxic cristae widening was phylogenetically developed in order to establish a partially dormant oxidative phosphorylation (OXPHOS) in typical glycolytic cancer cells [44,45]. Their metabolic signature lies in the mixed aerobic glycolysis and OXPHOS. The efficiency of ATP-synthesis decreased upon the hypoxic adaptation of HepG2 cells. The parallel HIF-induced phosphorylation led to an inhibition of the pyruvate dehydrogenase, and completely eliminated pyruvate entry into the Krebs cycle [44]. Note that besides being converted to lactate, pyruvate also bypasses a large part of the Krebs cycle, being used in glutaminolysis for transamination and thus providing 2-oxoglutarate [44–47]. In contrast, aglycemic cells metabolizing galactose and glutamine (being forced to conduct OXPHOS in this way, hence termed O_{XPHOS} cells) did not significantly diminish their respiration, and OXPHOS declined only slightly in parallel with intermediate increases in cristae width [44]. However, the inhibition of transaminases in hypoxic aglycemic HepG2 cells led to a non-canonical HIF-mediated restoration of the Krebs cycle and respiration connected to OXPHOS [45].

It remains to be established whether the process leading to the opposite morphology changes, i.e. to cristae narrowing, results from the net reversal of the widening mechanism or from an entirely different mechanism. We have attempted to elucidate this in this work.

2. Materials and methods

2.1. Materials

Reagents were from Sigma-Aldrich (St. Louis, MO), unless stated otherwise.

2.2. Cell cultures setting three distinct metabolic modes and hypoxic cell adaptation

Human hepatocellular carcinoma HepG2 cells were purchased from the European Collection of Authenticated Cell Cultures (ECACC 85011430). Cells were cultivated at 37 °C in a humidified incubator with 5% CO_2 in glucose-free DMEM (Thermo Fisher Scientific, Waltham, MA; formerly Life Technologies) supplemented with 3 mM glutamine, 10% (v/v) fetal calf serum (Thermo Fisher Scientific), 10 mM HEPES, 100 IU/ml penicillin, and 100 μg/ml streptomycin, and mostly with 5 mM glucose [44,45], but with 25 mM glucose or without glucose in the presence of 10 mM galactose in selected cases. Hypoxia was established using a SCI-tive N workstation (Ruskinn, Pencoed, UK) under 5% O_2 (~40 mm Hg; O_2 replaced with nitrogen) and 5% CO_2. Live cells were stained with Trypan Blue (Thermo Fisher Scientific, T10282), detached by trypsinization, and counted. Thus, 10 μl aliquots were mixed with 10 μl of Trypan Blue. The viability was then estimated using a Cell Counting Chamber and Cell Counter (Thermo Fisher

Scientific).

As previously described, HepG2 cells cultured with 5 mM glucose plus glutamine exhibited a mixed metabolism with the ATP production supplied by OXPHOS (including glycolysis) plus ATP production provided by (aerobic) glycolysis [44,45]. Upon cell culturing under mild hypoxia (5% O_2), the peak of HIF-1α protein stabilization was reached after 5 h [44].

2.3. High-resolution respirometry and ATP quantification

Cellular O_2 consumption was measured in the culture medium using an Oxygraph-2 k (Oroboros, Innsbruck, Austria) after air calibration and background correction [44,45]. Oxygen sensors were calibrated routinely at ambient air saturation and in oxygen-depleted media. A standard correction was performed for instrumental background oxygen flux arising from the oxygen consumption of the sensor and back-diffusion into the chamber. Respiration was measured at different cell densities at 37 °C in 2-ml chambers containing culture medium and expressed as O_2 flux *per* 10^6 cells in pmol $O_2 \cdot s^{-1} \cdot 10^{-6}$ cells. Cellular respiration was evaluated in intact cells (termed endogenous, "endo"). Non-phosphorylating (or leak) respiration („oligo") was obtained with oligomycin (2 μg/ml, Sigma-Aldrich, O4876). Maximum (uncoupled) respiration (max) was measured with the uncoupler (titrated by 0.5 μM steps up to 1.5–3 μM FCCP, carbonyl-cyanide p-(trifluoromethoxy) phenylhydrazone) (Sigma-Aldrich, C2920), reflecting the maximum kinetic capacity of the electron transport system, used for normalization. Inhibition with 100 nM rotenone (Sigma-Aldrich, R8875) plus 1 μM KCN or 2.5 μM antimycin A (Sigma-Aldrich, A8674) quantified the oxygen consumption unrelated to mitochondria (~5% of max), which was subtracted from each value. The ATP synthesis intensity is proportional to the endo/oligo ratios. To estimate the contribution of the nitric oxide synthase, which may inhibit respiration, the nitric oxide synthase inhibitor 2-(4-carboxyphenyl)-4,4,5,5-tetramethylimidazoline-1-oxyl-3-oxide (CPTIO) (Sigma-Aldrich, C221) was added to parallel measurements. An ATP Bioluminescence Assay Kit HSII (Roche, 11699709001) was used for relative ATP quantification.

2.4. Blue native electrophoresis and Western blotting

ATP-synthase oligomers and MICOS-SAM complexes were quantified by 3%–13% gradient gel blue native electrophoresis followed by the immunochemistry of mitochondria isolated from HepG2 cells (200–500 μg protein solubilized by 0.5%–1% digitonin for 30 min) (digitonin from Millipore, 300,410-1GM) or alternatively from cell lysates. For Western blotting, proteins were extracted by cell lysis in 50 mM HEPES, 150 mM NaCl, 1 mM EDTA, 1% Triton TX100, 1 mM phenylmethylsulfonyl fluoride, pH 7.4, and the amounts were quantified using BCA (Pierce, Rockford, IL, cat No. 23223). Separated proteins on SDS-polyacrylamide gels were transferred by *semi*-dry electroblotting onto PVDF membranes, then treated with the primary antibodies against the ATP-synthase α-subunit (Abcam, Cambridge, UK, ab14748), followed by secondary (horseradish peroxidase-conjugated) antibodies. ECL detection was accomplished with an Amersham blotting kit (GE Healthcare Bio-Sciences Corp., Piscataway, NJ) The ECL light intensity was quantified by densitometry using the software Scion Image beta 4.02 Win.

2.5. 3D imaging by super-resolution BiplaneFPALM microscopy

HepG2 cells were seeded on poly-L-lysine-coated coverslips (Paul Marienfeld GmbH, Lauda-Königshofen, Germany). HepG2 cells were transfected with the pLenti6.3-C-EOS-V5-DEST vector containing the subcloned fragment of 1–204 of mouse lactamase-β ($LACTB^{tr}$), an ICS-localized protein [48]. The expressed truncated $LACTB^{tr}$ conjugated with the photoconvertible Eos protein served as the inner membrane space marker, predominantly contouring the ICS volume [1]. For hypoxic samples, cells were transfected after 24 h in hypoxia. Dm2OG was added 10 min prior to fixation. Alternatively, cells were transfected with the pLenti6.3-C-EOS-V5-DEST vector containing a truncated sequence of FIS1 protein ($FIS1^{tr}$) to serve as an OMM marker [1]. Cells, fixed with 4% paraformaldehyde and 0.05% glutaraldehyde (both EMS, Fort Washington, PA, cat. No. 15714 and 16320, respectively), were imaged with a BiplaneFPALM instrument (Bruker, formerly Vutara Inc., Salt Lake City, UT), a prototype described elsewhere [1,42,43]. The biplane mode acquires two images of the sample at different focal planes simultaneously [42]. Usually 7000 to 10,000 frames were taken during acquisition. Photoconversion was performed using a 405 nm laser and Eos fluorescence was excited with the 561 nm laser. Diameter screening along the mitochondrial network reticulum length was done by transferring data via an image filter with Gaussian smoothing into the software Amira 5.5 (FEI, Visualization Science Group, Burlington, MA, currently Thermo Fisher Scientific), employing the sequence of algorithms of the Auto Skeleton module.

The IBM contour of mitochondrial network tubules was represented by blurred Eos-$LACTB^{tr}$ 3D images. The diameter d_{ICS} was obtained by the Auto Skeleton function at each selected i-th segment of mitochondrial network tubules. The Auto Skeleton first calculates an inter-distance map of the segmented image and then smoothes apparent tubing so that a string of connected voxels remains. Hence, the number of localized points in the blurred Eos-$LACTB^{tr}$ 3D images of each segment is converted to d^i_{ICS}, while the conversion of thicker blurred cristae is transferred to the larger d^i_{ICS} [1]. Histograms displaying the number of segments at each chosen range of d_{ICS} values were then constructed.

2.6. 3D super-resolution imaging by dSTORM

To visualize the protein of choice by 3D immunocytochemistry, direct stochastic optical reconstruction microscopy (dSTORM) was performed, using the same Vutara apparatus, again by taking 7000 to 10,000 frames [1,43]. Cells were fixed with 4% paraformaldehyde for 10 min, washed twice in PBS, permeabilized with 0.1% Triton X100, and the background was blocked by incubation for 15 min with buffered 5% BSA (for *anti*-Mic60 and *anti*-Samm50) or in 5% Donkey serum (Jackson ImmunoResearch, West Grove, PA). *Anti*-mitofilin/Mic60 (Abcam, ab110329), *anti*-SAMM50 (Sigma-Aldrich, HPA034537), *anti*-OPA1 (BD Biosciences, 612606), or Alexa-Fluor-647-conjugated *anti*-ATP-synthase α-subunit monoclonal antibodies (Abcam, ab196198) were separately used (0.5 μg/ml) for 1 h with constant shaking. Coverslips were then washed three times in PBS. For unconjugated antibodies, one-hour incubation in PBS with Alexa-Fluor-647 secondary antibody (Thermo Fisher Scientific, A31573) was followed by triple washing with PBS. Samples were mounted in "dSTORM buffer" (10% glucose, 169 units of glucose oxidase, 1.4 units of catalase all in a buffer containing 10 mM NaCl, 50 mM mercaptoethanol, 50 mM Tris-HCl, pH 8.0).

For double-channel (i.e. double-color) dSTORM, the second antigen was similarly visualized using a Cy3B-conjugated secondary antibody that we prepared from donkey *anti*-rabbit IgG (Jackson ImmunoResearch) by reaction with the monoreactive dye Cy3B NHS ester (GE Healthcare, Bio-Sciences Corp., Piscataway, NJ, cat. No. PA63101) in 100 mM sodium bicarbonate, pH 8.5, for 2 h. The product was purified in an Illustra NAP-5 Sephadex G-25 column (GE Healthcare) equilibrated with PBS, pH 7.4.

2.7. Histogram analysis of 3D inter-distances between antibodies

Repeating features in the mitochondrial ultramorphology can be described by the most frequent distances (MFDs) [43]. Thus, when we want to simplify a crista to a cylinder, the MFD should be near to its diameter. A more realistic model would be represented by two parallel planes of a cuboid (opposite enfolded IMM). In this case, the MFD is near to the distance between these two planes (the relevant cuboid

size). The pointilistic character of stochastic 3D microscopy images theoretically enables the inter-distances between all localized points to be determined and listed. Repeating features of the analyzed biological sample should then be manifested as local maxima in the histogram of such inter-distances [43]. The inter-distance histogram can be derived on the basis of 3D Ripley's *K*-function as outlined below.

A cumulative frequency function (cumulative distribution function) $H(r)$ is defined as counting for a given r for all distances between points shorter than r:

$$H(r) = \sum \sum^{n}_{i<j} d_{ij} = ½ \sum \sum^{n}_{i\neq j} d_{ij}, \quad (1)$$

where $d_{ij} < r_{max}$ are distances between points i and j (note, when d_{ij} is identical to d_{ji} and $i = j$ those distances are excluded). The limit r_{max} exists, corresponding to $H(r) = N^{rmax}$, in which all distances are counted. The number of all distances $N^{rmax} = n(n-1)/2$ for the existing number of points n and r_{max} is simply the longest distance between points.

The 3D Ripley's *K*-function then expresses the expected number of events (points) within the distance r from a randomly selected point [49]. Let's assume a volume of interest in which n points (events) exist with distances d_{ij} (point i, point j). 3D Ripley's *K*-function can then be expressed [50,51] for the value $K(r)$, denoting how many points become encircled within a sphere of radius r:

$$K(r) = V \cdot n^{-2} \cdot \sum \sum^{n}_{i\neq j} \delta_{ij}, \quad (2)$$

where the indicator function $\delta_{ij} = 1$ if distance d_{ij} (point i, point j) $\leq r$, otherwise $\delta_{ij} = 0$.

Comparing $K(r)$ to a completely spatially random (CSR) case, for which $K_{CSR}(r) = (4/3)\cdot\pi\cdot r^3$ (i.e. a volume of a sphere of radius r), the *L*-function normalized for the average point (event) density is defined as:

$$L(r) = (3K(r)/4\pi)^{1/3} \quad (3)$$

This can be used to compare the calculated $L(r)$ vs. the chosen diameter r. As a result, the meaning of the $L(r)$ - r function is that a cluster value is ascribed to every voxel of a volume V, while such a value is relative to the expected case of a completely spatially random (CSR) case. When values $L(r) - r > 0$ occur, clustering is indicated; when $L(r) - r < 0$ the regular (ordered) pattern exists. Obviously, when $L(r) - r = 0$, the situation indicates a case of CSR.

The Ripley's *K*-function is related to the cumulative frequency function $H(r)$ as follows:

$$K(r) = 2 \cdot V \cdot n^{-2} \cdot H(r), \quad (4)$$

since the number of events and the number of distances differ only in that the Ripley's function counts them twice. Consequently, the histogram of (inter)distances described by the function $H(r)$ can be derived from the 3D Ripley's *K*-function using the consideration of scanning within the 3D space as follows:

For each point k, the list of distances centered on k is gathered and sorted so that distances are shorter than r and counted to obtain their sum $\mathscr{L}_k(r)$. Scanning over all points (summation over all points k) for $r \leq r_{max}$, the cumulative function $\mathscr{L}(r)$ is obtained. To avoid data explosion, a table can be constructed of $\mathscr{L}(r)$ values vs. a stepwise r, with a step of ε. The resulting table will thus contain values given by $\mathscr{L}(\varepsilon)$, $\mathscr{L}(2\varepsilon)$, … $\mathscr{L}(n\varepsilon = r_{max})$ plotted vs. ε, 2ε, 3ε, … $n\varepsilon = r_{max}$. Subsequently, a *histogram of distance frequency distribution* with a bin of length ε can be constructed. As a result, we can plot differences $\{\mathscr{L}(n\varepsilon = r_{max}) - \mathscr{L}(n\varepsilon-\varepsilon)\}$; $\{\mathscr{L}((n-1)\varepsilon) - \mathscr{L}((n-1)\varepsilon-\varepsilon)\}$; … $\{\mathscr{L}(2\varepsilon) - \mathscr{L}(\varepsilon)\}$ vs. $\{n\varepsilon\}$, $\{(n-1)\varepsilon\}$, …$\{2\varepsilon\}$. In 2D, this procedure amounts to scanning an image using a circular ring (annulus) with a thickness of ε. For 3D images this is represented by scanning the 3D image as a spherical shell with a thickness of ε. Because of the relation of Eq. (4), such a histogram should provide the same local maxima as the histogram of plain "inter-distances" d_{ij} within the sphere r_{max}.

Calculations of the 3D Ripley's *K*-function ($\mathscr{L}(r)$ function) from the localized points by dSTORM imaging were done using the software package Vutara [43]. Adopting the above-described procedures, histograms of plain "inter-distances" between *loci* occupied by the chosen antibody molecules were constructed. Usually MFDs were judged from the local maxima existing in the resulting histograms that ordered all the inter-distances between the localized single antibody molecules. Either a single MFD was listed to characterize each image; or a detailed comparison between the two histograms for 3D images of two different samples was used by simply dividing the first histogram by the second one. The resulting variation function was plotted for all combinations comparing two series of 3D images.

2.8. Transmission electron microscopy

HepG2 cells were cultured on L-poly-lysine-coated Petri dishes. For transmission electron microscopy (TEM), cells were fixed for 24 h in 2.5% glutaraldehyde in 0.1 M cacodylate buffer (pH 7.2) and *post*-fixed in 2% OsO_4 (EMS, 19170) in the same buffer. Fixed samples were dehydrated through an ascending grade of ethanol and embedded in an Araldite - Poly/Bed® 812 mixture. Thin sections were cut in a Reichert-Jung Ultracut E ultramicrotome and stained using uranyl acetate and lead citrate. Sections were examined and photographed using a JEOL JEM-1011 electron microscope. Fine structure measurements were performed using a Veleta camera and iTEM 5.1 software (Olympus Soft Imaging Solution, GmbH).

Alternatively, high-pressure freezing preceded TEM imaging, essentially as described elsewhere [1]. Briefly, the sapphire discs were transferred to copper membrane carriers (Leica, Mannheim, Germany) and the cells in the medium containing 20% BSA were immediately frozen in a Leica EM PACT high-pressure freezer. Frozen samples were transferred to a Leica AFS machine and freeze-substituted in acetone (EMS, Hatfield, PA; glass distilled) containing 1% glutaraldehyde (EMS, 10% stock in acetone), 0.33% OsO4 (Polysciences, Warrington, PA), 1% uranyl acetate (Polysciences; 20% methanolic stock) and 1% water. The substitution protocol included 24 h at −90 °C, temperature elevation (+5 °C/h) to −40 °C; 12-h incubation at −40 °C, washing 4-times with pure pre-cooled acetone at −40 °C; infiltration with Lowicryl HM20 resin (3:1, 1:1, 1:3 (v:v) acetone:HM20 mixtures for 2 h each); and incubation for 2 h in 100% HM20 in a fresh resin, left to polymerize with UV light for 24 h at −40 °C and ~3 days at 20 °C. Ultrathin resin sections (60 nm) were cut with an Ultracut S ultramicrotome equipped with a diamond knife (45°; Diatome, Hatfield, PA) and placed on formvar-coated copper grids. The sections were contrasted with a saturated aqueous solution of uranyl acetate for 1 h, washed, air-dried and examined in a FEI Morgagni 268(D) transmission electron microscope at 80 kV (FEI). Images were captured with a Mega View G2 CCD camera (Olympus, Center Valley, PA).

2.9. Focused ion beam/scanning electron microscopy

Samples for FIB/SEM tomography were stained with rOTO (reduced osmium tetroxide-thiocarbohydrazide-osmium tetroxide), based on ref. [52], followed by staining with 1% uranyl acetate (SERVA, SERV.7787002) to enhance tissue contrast. The Epon block was mounted on regular SEM stubs using conductive carbon and coated with 25 nm of platinum (using High Vacuum Coater, Leica ACE600). Ion milling and image acquisition was performed in a FEI Helios NanoLab 660 G3 UC dual beam system (Thermo Fisher Scientific, MSD, Hillsboro, OR, USA; and MSD, FEI, Brno, Czech Republic). A large trench was milled at a current of 21 nA and 30 kV, followed by fine milling at 0.79 nA and 30 kV, the thickness of slices was 5 nm. The platinum layer was 1000 nm on top of the surface using the single gas injection system of the FIB/SEM. SEM images were acquired at 2 kV and 0.2 nA using an InColumn backscattered electron detector, dwell time of 25 µs. The pixel size was set to 3.9 nm.

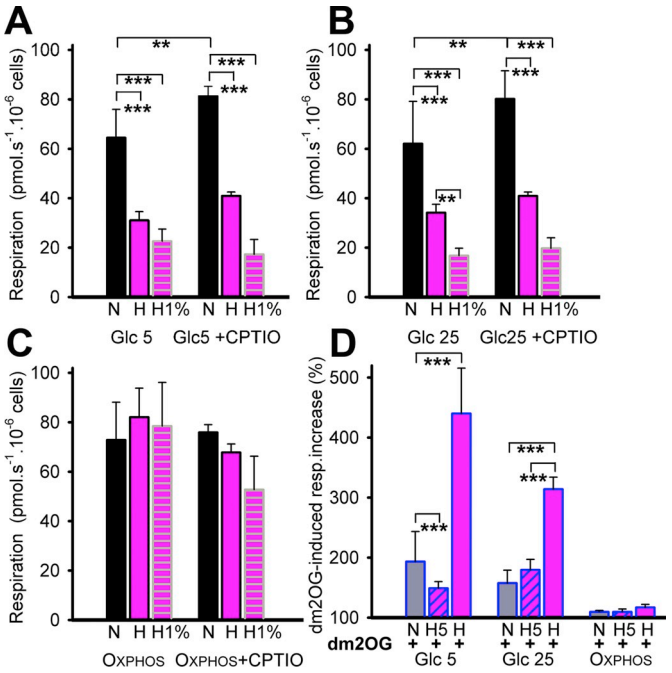

Fig. 1. Respiration of HepG2 cells in atmospheric, 5% and 1% oxygen and its acceleration upon the addition of dm2OG.

Glycolytic HepG2 cells cultivated with 5 mM glucose ("Glc 5") (**A**), 25 mM glucose ("Glc 25") (**B**), and in the strict absence of glucose replaced with galactose (aglycemic "OXPHOS" cells) were cultured at normoxia ("N") and under 5% O_2 ("H") or 1% O_2 ("H1%") hypoxic conditions for 72 h and assayed by oxygraph under the corresponding normoxic/hypoxic oxygen concentrations in the absence or presence of CPTIO (an inhibitor of nitric oxide synthase) as indicated. The rate of respiration (mean ± SD) is shown for five independent cell cultures of each metabolic mode, including three 5% O_2 and three 1% O_2 hypoxic incubations and 15–20 assays for normoxia and 5–12 for hypoxia (3–6 with CPTIO), except for "HN", which consisted of 4 assays. D) Relative increase in respiration immediately after the addition of 4 mM dm2OG. Here "H5" denotes 5 h of incubation at 5% oxygen, otherwise "H" was 72 h of incubation. Number of assays $n > 6$. ANOVA Tukey's test: $^{**}P < 0.05$; $^{***}P < 0.001$ Differences among data for OXPHOS cells were statistically insignificant.

2.10. Statistical analysis

ANOVA, using SigmaStat 3.1 (Systat Software, Chicago, IL), was carried out with subsequent pairwise multiple comparisons (Tukey's test) or Kruskal-Wallis analysis on ranks with Dunn's test.

3. Results

3.1. Dormant mitochondria in hypoxic glycemic HepG2 cells have a shortage of substrate for entry into the Krebs cycle and respiratory chain

We previously found that glycolytic HepG2 cells diminished their endogenous respiration down to 45% after a hypoxic 72-h adaptation to 5% O_2 [44,45]. In this work, we expanded those measurements to obtain the maximum "endo" respiration without any possible inhibitory contribution of the nitric oxide synthase, since the resulting nitric oxide inhibits respiration. This was eliminated with the nitric oxide synthase inhibitor CPTIO. After 72-h hypoxic adaptation at 1% ("H1%") and 5% oxygen ("H", Fig. 1A–C) glycolytic cells, cultivated and tested with 5 mM and 25 mM glucose, profoundly reduced their respiration (Fig. 1A,B). Such respiration did not recover, when cells were placed back in ambient atmospheric conditions [44]. In contrast, aglycemic "OXPHOS" cells cultivated with galactose and glutamine did not decrease their respiration even at 1% oxygen (Fig. 1C; values appeared slightly lower, but this was insignificant). The metabolism of OXPHOS cells relies on glutaminolysis plus the Leloir pathway of galactose [45]. The latter consumes a majority of glycolytic ATP, hence in order to survive cells must maintain their OXPHOS. Also, notably, irrespective of the metabolic mode, cells exhibited the same maximum endogenous respiration, when corrected for nitric oxide synthase inhibition.

To ensure an unlimited availability of OXPHOS substrate, we employed a cell membrane permeable analog of 2-oxoglutarate, dimethyl-2-oxoglutarate (dm2OG). When dm2OG was added to already hypoxia-adapted glycolytic HepG2 cells cultured with 5 mM glucose after 72 h at 5% O_2, an immediate increase in their respiration occurred (Fig. 1D), up to 9-fold (± 1.7-fold) vs. hypoxic values (~4.4-fold vs. normoxic values). Similar increases were found for cultivation with 25 mM glucose. Note that this increase was not observed for aglycemic, i.e. OXPHOS cells, which apparently reached the maximum Krebs cycle turnover. The respiration increase of glycolytic HepG2 at normoxia was up to 1.9-fold (± 0.5-fold) with 5 mM glucose. Since the hypoxic widening of aglycemic cells was to a lower extent [1], we employed HepG2 cells cultivated, adapted and assayed with 5 mM glucose in subsequent experiments, unless stated otherwise.

3.2. Cristae narrowing at faster metabolism due to dimethyl-2-oxoglutarate load

We attempted to elucidate whether cristae morphology is affected by a sudden increase in 2-oxoglutarate (substrate) load. Samples for TEM were casted prior to and 10 min after the addition of dm2OG to hypoxia-adapted or normoxic glycolytic HepG2 cells. We also attempted to distinguish whether cross-sections of mitochondrial network tubules were imaged (Fig. 2Aa) or whether the imaged cross-sections originated from mitochondrial ~2 µm spheroids fragmented from the main network (Fig. 2Ab). Mitochondrial tubules and bulky spheroids were identified by 3D super-resolution images of parallel samples, when visualized using the OMM marker $FIS1^{tr}$ (Fig. 2Aa,b). According to these images, typical tubule (OMM contour) diameters were ~600 nm (520–670 nm), which was also confirmed by FIB/SEM (see below; 540–670 nm). Examples of the resulting TEM images are shown in Fig. 2B–G, while panels Ba,Bb show the high-pressure-frozen samples.

Thus, random sections of mitochondrial network tubules, commonly termed "mitochondria" (Fig. 2Ba,Bb,Ca,Cb,Ea,Fa,Ga,Gb), as well as sections of up to 2.2 µm spheroids (Fig. 2Da,Db,Eb,Fb), frequently contained bulky inflated cristae in hypoxia-adapted cells (Fig. 2, all panels a). In contrast, all cristae were narrower when samples were taken shortly after the addition of dm2OG (Fig. 2, all panels b), or up to 2 h later. Their width was nearly equal to the cristae width found at normoxia (Fig. 3A,B).

The statistics of 20–60 analyzed sections with at least 12 estimates *per* section yielded the histograms shown in Fig. 3A,B with a weighted average of cristae width of 18.4 ± 9 nm prior to and 11.5 ± 3 nm after the addition of dm2OG to hypoxia-adapted cells; and 11.2 ± 3 nm in normoxic cells, or 11.8 ± 3 nm with dm2OG at normoxia (inset in Fig. 3A). The hypoxic cristae width distribution contained at least three populations peaking at 11, 18 and 35 nm (Fig. 3A). The wider cristae at hypoxia more frequently had a shorter length (Fig. 3C,E vs. D,F). This was also apparent as a lower aspect ratio within the ensemble of cristae (Fig. 3E,F). A model explaining why a crista's length has to be shortened upon crista widening is shown in Fig. 3G. The realistic character of this cuboid model is supported by the following: *i*) the existence of similar crista lamellae in FIB/SEM images (Fig. 3G); and *ii*) perfect fits of the dependence of the aspect ratio (l_2/w_2) to the reciprocal of the width squared ($\sim 1/w_2^2$) (Fig. 3E,F). Note that our model is valid in the absence of de novo IMM biogenesis, due to the conserved IMM surface (mass).

To understand the overall topology of mitochondrial cristae within segments of mitochondrial network tubules, we imaged cristae in HepG2 cells using FIB/SEM (yellow in Fig. 4A–E, see also

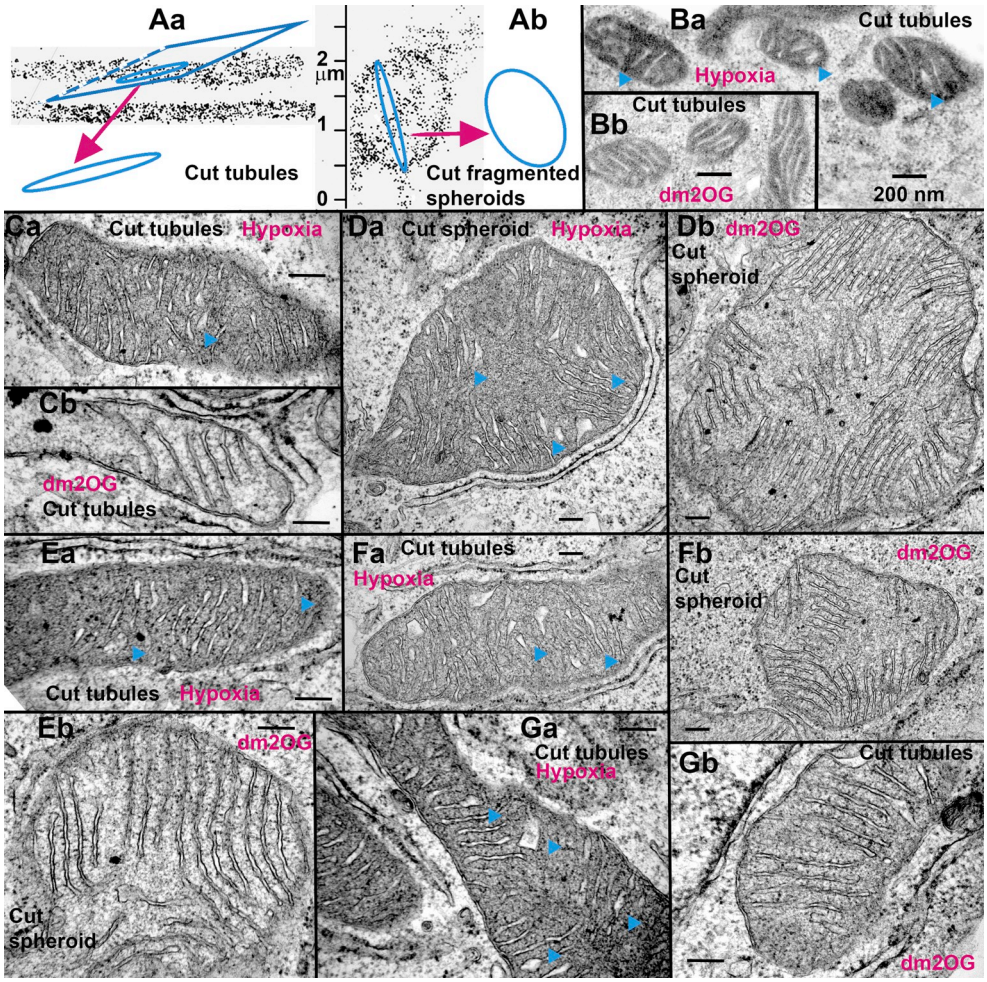

Fig. 2. Typical TEM images of cristae width after 72 h of 5% hypoxia without or with dm2OG-induced high substrate load in HepG2 cells.

A) Two possible types of sections of the mitochondrial network are illustrated, either dissecting tubules (Aa) or bulky spheroids (Ab); the latter being most frequently fragmented off the main mitoreticulum. The scheme uses authentic 3D images of the intact mitochondrial network visualized by 3D super-resolution FPALM of HepG2 cells transfected with truncated Eos-FIS1^{tr} and cultured with 5 mM glucose (Aa) or a fragmented network after treatment with 1 µM of the uncoupler FCCP (Ab). Each dot represents the fluorophore conjugated to the FIS1^{tr} molecule localized during the FPALM acquisition.

B–G) Typical TEM images of cryo-preserved (B) or traditionally stained (B–G) samples of HepG2 cells cultured with 5 mM glucose at hypoxia for 72 h (5% O_2) without further treatment (all panels a) and after 10-min incubation of hypoxia-adapted cells with 4 mM dm2OG (all panels b). Arrows indicate bulky inflated cristae. *Scale*: 200 nm.

Supplementary material, Movie 1). The diameter of OMM (green in Fig. 4A–E) was between 540 and 670 nm. Cristae appear as "lamelae" protruding perpendicularly by the entire OMM diameter but frequently tilted. The inner "cylinder" of IBM was clearly recognized. Crista junctions, i.e. outlets into the thin intermembrane space between the IBM and OMM, were apparent in the contacts with the IBM (red arrows in Fig. 4A–E). On average they were spaced ~90 nm apart, which was also confirmed by TEM (85 ± 25 nm). The apparent ~50–70 nm width (the shortest dimension) of these lamelae, representing cristae, is wider than the TEM sections. This fact can be explained either on the basis of staining by numerous layers of stains adding to the width of two parallel ~4 nm lipid membranes; or by the staining of supercomplexes of the respiratory chain. Located at the sharp edges of crista rims, rows of ATP-synthase dimers are expected with F_1 moiety "heads", uplifted by ~10 nm above the IMM. When these "heads" are stained, they would also add to the intermediate size (the distance *m* in Fig. 3G) of apparent cristae.

3.3. Crista width changes are reflected by the ICS marker contouring mitochondrial network tubules

3D BiplaneFPALM super-resolution microscopy can achieve a resolution of 25 nm in the xy-plane and 50 nm along the z-axis (perpendicular to the coverslip). Using the 3D BiplaneFPALM we imaged the Eos-LACTB^{tr} tubular contour of IBM (Fig. 5A–C). Despite not resolving cristae due to an insufficient resolution of BiplaneFPALM in the z-axis, the localized points in the blurred Eos-LACTB^{tr} 3D images were converted using the Auto Skeleton algorithms to the diameter d_{ICS} at each chosen segment along the entire mitochondrial tubular network. From this we constructed histograms of d_{ICS}. We previously verified that the thicker blurred cristae provide a larger apparent d_{ICS}, when cells were transfected during the hypoxic incubation [1]. Actually, the OMM contour did not change, whereas the ICS contour expanded in hypoxia, while the matrix contour shrunk [1]. We expected the opposite changes upon the dm2OG load, so we constructed histograms of d_{ICS}. This procedure enables various samples to be compared (Fig. 5D).

When hypoxia-adapted glycolytic HepG2 cells were supplemented for 10 min or 2 h with dm2OG (Fig. 5C), lower apparent d_{ICS} values were indicated by the histograms than for the hypoxic samples. The histograms of dm2OG-treated hypoxia-adapted cells were nearly identical to those for normoxic cells (not shown). Gaussian fits of the resulting histograms yielded the most frequent diameter d_{ICS} values (± 0.5 FWHM) of 267 ± 28 nm and 243 ± 39 nm for cells prior to and after the addition of dm2OG, respectively. Normoxic cells prior to the hypoxic adaptation exhibited the most frequent diameter d_{ICS} of 234 ± 33 nm. This was actually lower than the OMM contour, estimated by FIS1^{tr} images (Fig. 2A) or FIB/SEM (Fig. 4A–E). We can conclude that the addition of the instant permeable substrate to glycolytic hypoxia-adapted cells reverses their hypoxic ICS expansion [1].

3.4. Cristae morphology changes derived from 3D dSTORM immunocytochemistry of $F_1\alpha$-ATP-synthase

Next, we employed our novel approach based on stochastic 3D dSTORM super-resolution microscopy [43]. We performed analyses of histograms for 3D inter-distances between the chosen primary antibodies, when histograms are derived from the Ripley's K-function of 3D images such as in Fig. 6A,B. The primary antibodies against the α-

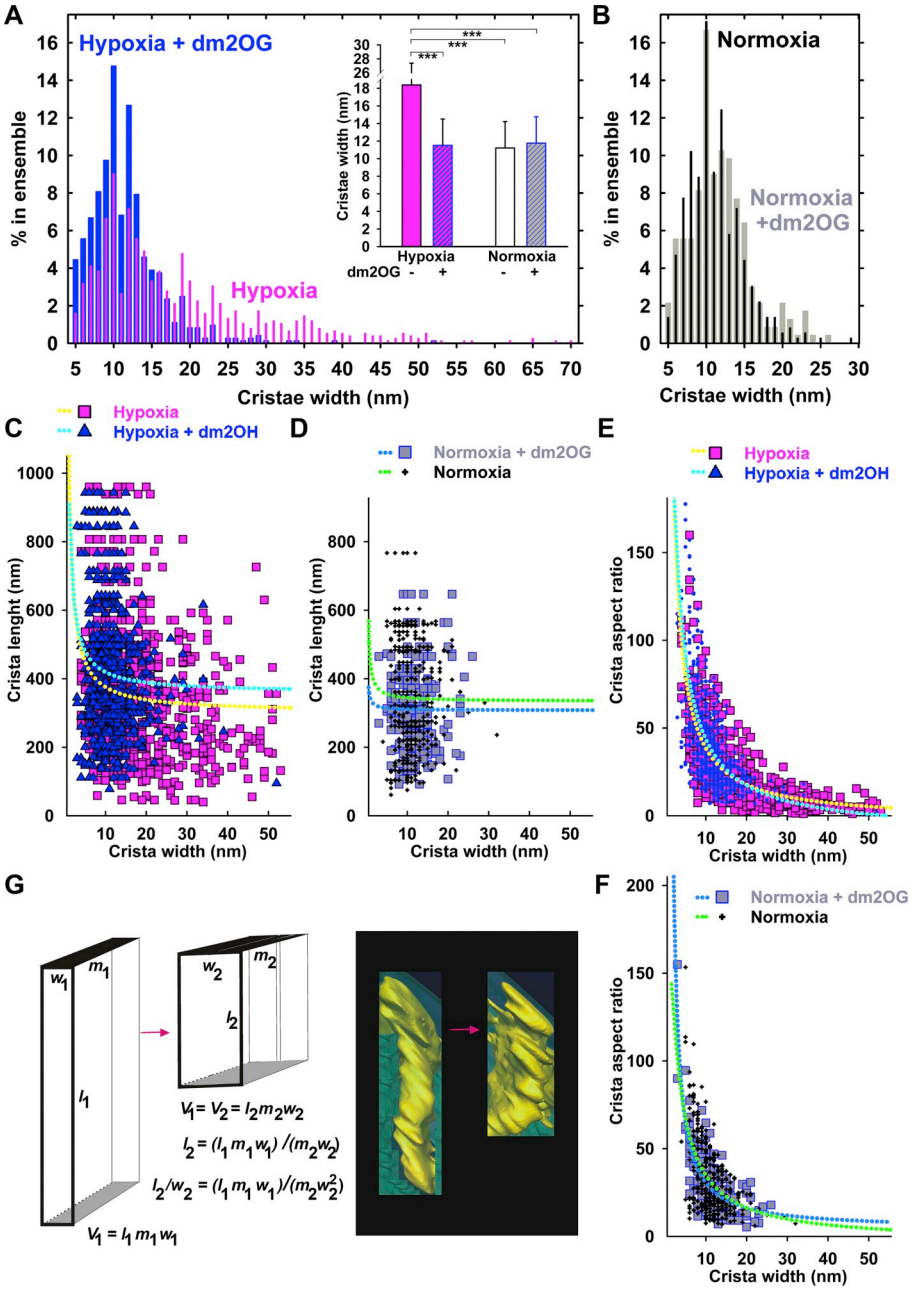

Fig. 3. Histograms of cristae width (A, B) and resulting correlations (E–F) on the basis of simple cuboid model (G).

A, B) Histograms were derived from 10 to 30 TEM images for each sample as in Fig. 2B–G, containing up to 3 mitochondrial network tubule cross-sections with a total of 120–360 estimations of cristae sections: *Black bars or symbols* (*white bar* in inset of **A**): normoxia*; gray bars or symbols*: normoxic 10-min incubation with 4 mM dm2OG; *pink bars or symbols*:72-h hypoxia-adapted cells at 5%O_2; *blue bars or symbols* (*dashed blue & pink* in inset of **A**): hypoxia-adapted cells after 10-min incubation with 4 mM dm2OG.

C, D) Reciprocal correlation of crista length vs. crista width for individual cristae (*l* vs. *w*; fits to 1/width: *yellow* for hypoxia; *cyan* for dm2OG after hypoxia; *green* for normoxia, *blue* for normoxia plus dm2OG).

E, F) Quadratic reciprocal correlation of corresponding aspect ratios vs.1/width^2. Fits to 1/width^2 were done using the same color coding. G) *Right part*: Cuboid 3D model of crista (without a crista outlet) and its changes from state 1 (cuboid of dimensions w_1, m_1, l_1) to state 2 (cuboid of dimensions w_2, m_2, l_2), including the equations for crista length and aspect ratio changes. *Left part*: Authentic cristae taken from FIB/SEM images such as displayed in Fig. 4.

subunit of the ATP-synthase F_1 sector ($F_1\alpha$) conjugated with the Alexa Fluor 640 fluorophore was our first choice (Fig. 6A,B), since these markers may be exposed up to ~20 nm above the ICS membrane (Fig. 6C,E). In this way, these immune markers transfer the indistinguishable distances *m* ("medium" size of lamellae) into distances suitable for our 3D resolution of ~30 nm [43]. Our model in Fig. 6C derived the intermediate dimension of cristae lamellae *m* from the measured average cristae width *w* ("TEM width") of 18-nm at hypoxia vs. 11-nm distance after dm2OG (inset in Fig. 3A). Note that *m* represents a distance between the parallel ICS membrane rims of cristae. Alternatively, when antibodies would bind simultaneously to both monomers in a single dimer (Fig. 6Cb), which is rare, distances representing the top extent of such a "V" shape may be mixed with the representative distances *m* between the two rims covered by ATP-synthase dimers (Fig. 6E).

The typical resulting histograms indicate that the statistically lower $F_1\alpha$ inter-distances, taken in 3D, exist in normoxic HepG2 cells when compared to hypoxia (7Aa,b). The most frequent distance (MFD) may be proportional to the average distance between the ATP-synthase rows at the opposite rims of cristae membranes (Fig. 6D), i.e. the distance *m* ("medium" size of lamellae). This is valid unless distances within a single ATP-synthase dimer predominate in the data set, which is quite unlikely. As a result, we interpret that the decreased MFD can reflect the shortening of the distances between the rims (edges of crista lamellae containing rows of ATP-synthase dimers). Similarly to the 2D model (Fig. 6Ca,b), the shortening of the longer distance of the lamellae "bag" must lead to a shortening of its shortest distance, i.e. the transversal width *w* (Fig. 3G) and most likely also the medium size *m*. In this way the increasing/decreasing MFD or even the proximal data around MFD reflect changes in cristae morphology and their transversal width and distance between edges (rims).

After 72 h of hypoxic adaptation at 5% O_2, the average MFD increased by 12 nm (Fig. 6D) and the corresponding histograms indicated a higher proportion of longer $F_1\alpha$ inter-distances (Fig. 7A). This reflects a higher fraction of wider cristae existing in vivo. In contrast, after the addition of dm2OG to hypoxia-adapted HepG2 cells and 10 min

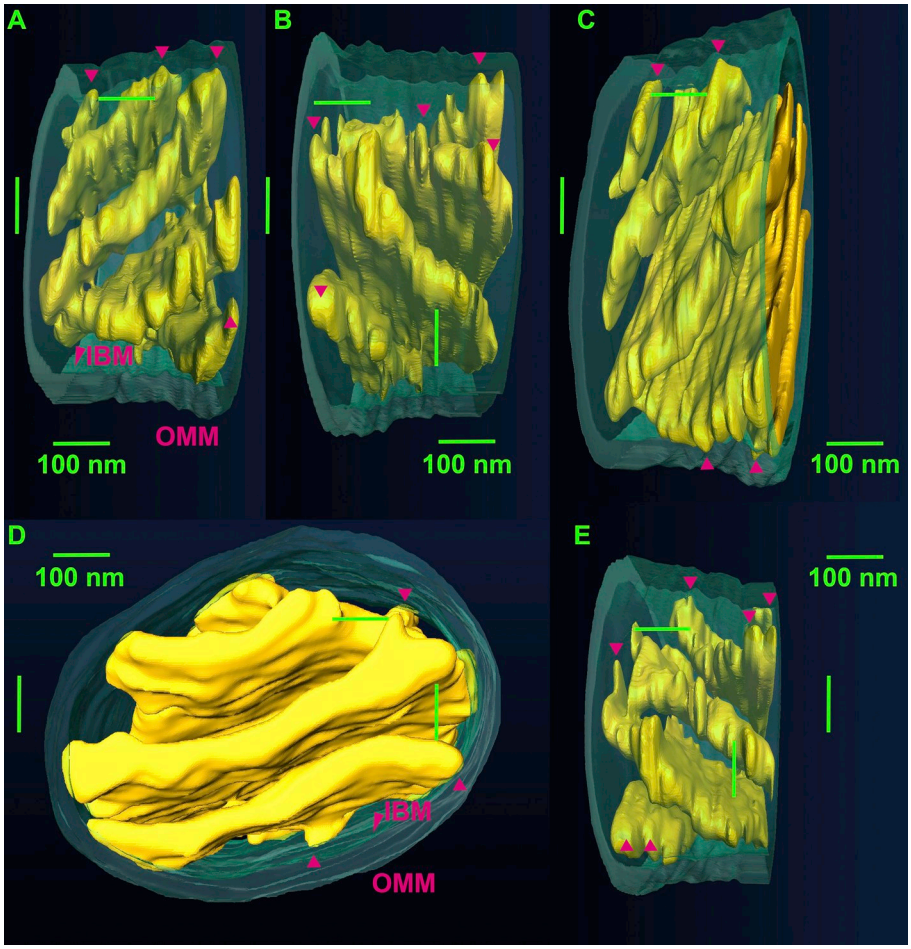

Fig. 4. FIB/SEM.
Focused ion beam/scanning electron microscopy – 3D images of several segments of mitochondrial network tubules are displayed after image reconstruction using the software Amira 5.5 (A–E). See also Supplementary material, Movie 1. The outer membrane (OMM, *translucent green*) and inner boundary membrane (IBM, *more intensive green*) are clearly visualized together with the cristae lamellae (*yellow*). The red arrows indicate the crista junctions, i.e. the outlets of the cristae lumen to the intermembrane space between the OMM and IBM. Note that both the IBM and intracristal membrane are continuous portions of the IMM.

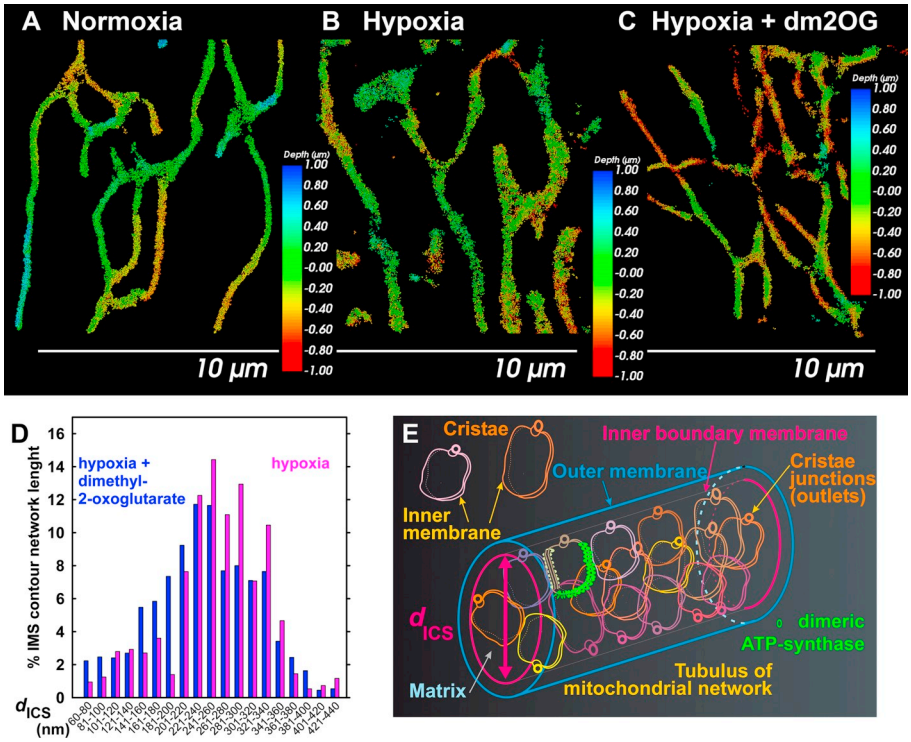

Fig. 5. ICS volume decrease upon high substrate load. A–C) Typical projections of 3D super-resolution PALM images of Eos-lactamase-β, color-coded for depth (z-axis). **D**) Histograms of diameter distributions, sampled along the Eos-lactamase-β- visualized tubular contour of the mitochondrial network in HepG2 cells, is shown for hypoxia (72 h, 5%O_2; *pink bars*), and hypoxia-adapted cells after 2-h incubation with 4 mM dm2OG (*blue bars*). The diameters of the IMS contour (in fact the ICS contour, due to the negligible thickness of the intermembrane space between the OMM and IMM) were derived from 10 to 12 cells. Sampled diameters d_{ICS} of cylindrical segments of the contour along the whole mitoreticulum (obtained by cylindrical modeling using the Auto Skeleton routine of Amira 5.5) were sorted along the histogram x-axis into 20-nm groups for d_{ICS}. Their occurrence is shown, expressing how much % each group segment length relates to the 100% length of the whole Eos-LACTB^{tr}-visualized mitochondrial reticulum in a single cell. E) Scheme of idealized cristae morphology within segment of mitochondrial tubule. The "flat bottles" represent the simplest crista model as if all cristae had the same dimensions. In reality the cristae length may span nearly the whole IBM diameter. Note that the rows of ATP-synthase dimers form the edge (crista rims). The crista width *w* is then the shortest size (illustrated by parallel lines), the inter-rim distance is the medium size *m* and crista length *l* is represented by the length of the bottle (the largest dimension, perpendicular to the IBM and OMM cylinder).

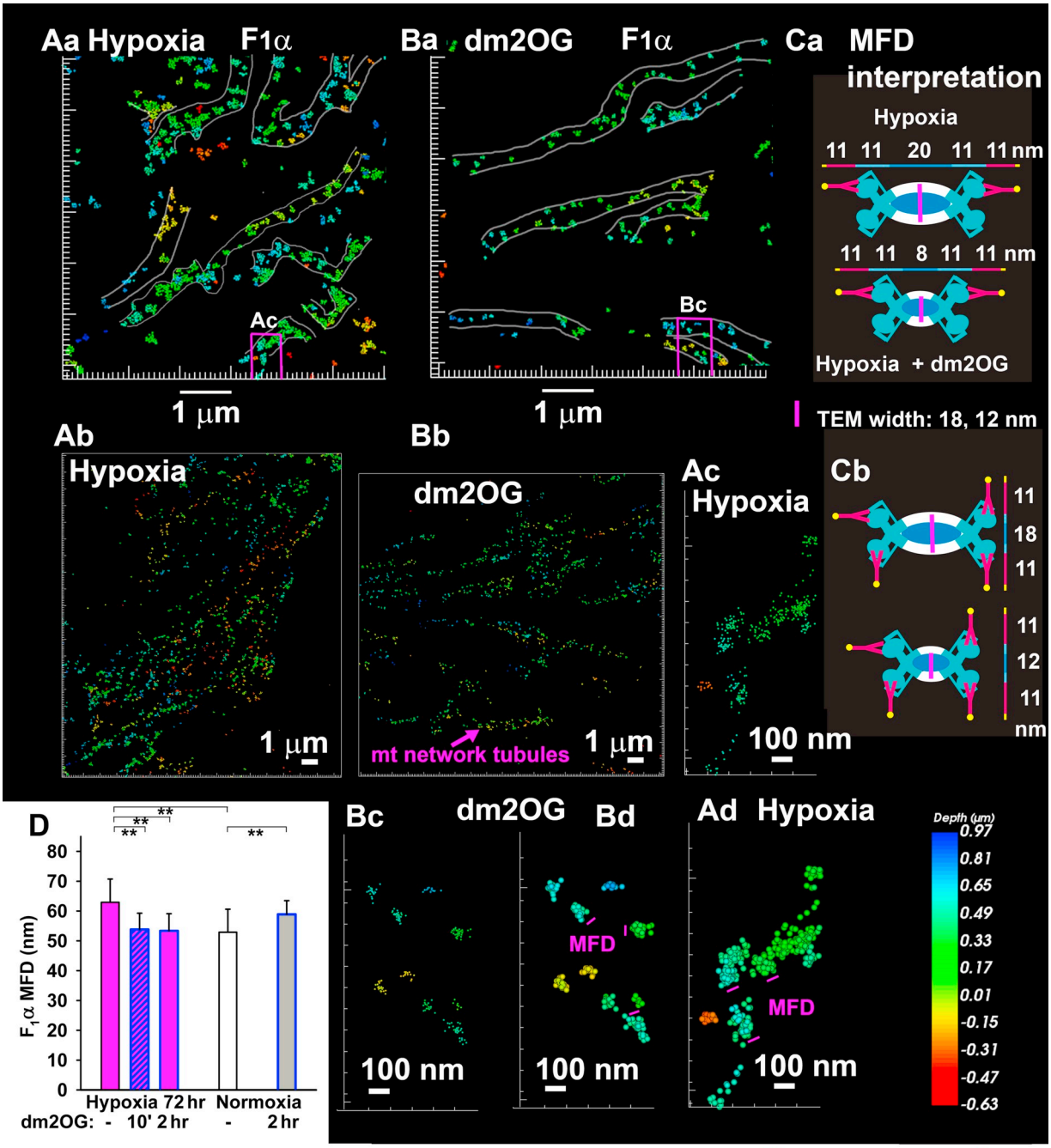

(caption on next page)

Fig. 6. ATP-synthase $F_1\alpha$ antibody inter-distances and interpretation of MFD.
A, B) Typical projections of 3D dSTORM images, representing 3D immunocytochemistry with primary Alexa Fluor 647-conjugated antibodies against the α-subunit of the ATP-synthase F_1 sector, after 72 h of hypoxia at 5% O_2 (A) and after subsequent 10-min incubation with 4 mM dm2OG (B). All panels b – projections of the entire wide-field image with the apparent IMM contours of the mitochondrial network tubules; all panels a – 6 × 6 μm projections with arbitrary drawn tubule portions; and panels c – detailed 0.6 × 1.2 μm projections (their locations are indicated by the pink frames in panels a). D) Resulting average MFDs, shown also for normoxic samples with and without dm2OG and the 2-h incubation of hypoxia pre-adapted cells with dm2OG.
C, E) Interpretation of the MFD between antibody fluorophores. Ca) Most plausible model in 2D: 20 and 8 nm inter-rim distances (*m*, between the two sharp edges of ICS membranes) are considered in this model for hypoxic conditions (top) and hypoxic conditions with the dm2OG substrate overload (bottom). An uplift of 11 nm above the center of the IMM [29,58] is taken for the F_1 sector α-subunit and 11 nm is considered for the additional antibody size including the fluorophore. Altogether these distances give inter-distances of 64 and 52 nm between fluorophores of $F_1\alpha$ antibodies, which are observed experimentally as the average MFDs (D). Cb) A model situation when both $F_1\alpha$-subunit "heads" are labeled with antibodies: this model gives MFDs of 40 nm (for 18 nm crista width – see Fig. 3A) and 34 nm (for 12 nm crista width – see Fig. 3A) in hypoxic and dm2OG-treated samples, respectively.
E) The most plausible model in 3D: Octamers, i.e. four sets of ATP-synthase dimers were modeled using the published structure [58] of the yeast *S. cerevisiae* ATP-synthase dimer (pdb code 6b8h), and created using the PyMOL Molecular Graphics System, Version 1.8.2.0 Schrödinger, LLC. *Left*: Mirrored octamers are attached to the cuboid model of the crista membrane at a medium crista-size distance "*m*" of 50 nm. *Right*: Mirrored octamers are tentatively covered with three IgG models containing fluorophores (red spheres). The resulting MFD of this model is indicated besides the V-span of the dimer, which is 30 nm.

(Figs. 6D, 7B) or 2-h incubation (Fig. 7B), a proportional reduction was observed for longer 3D inter-distances in the related histograms. This reflects the portion of wider cristae being diminished within the ensemble. We may conclude that when there is a high Krebs cycle substrate 2-oxoglutarate load (originating from the added dm2OG), the hypoxia-inflated cristae predominantly return to their original narrow width (Fig. S1A).

In order to provide a detailed analysis, next we divided histograms for hypoxic samples by those for normoxia for each distance step (Fig. 7C,D). Also, histograms for hypoxia were divided by those for the additions of dm2OG to hypoxic cells (Fig. 7E,F), and finally those for the additions of dm2OG at hypoxia were divided by those for normoxia (Fig. 7G,H). Panels E and G represent experiments in which dm2OG was incubated for 10 min, while the results in panels A, C, and E were measured in parallel; and the remaining panels show the results of the 2-h incubation with dm2OG. Statistically, the results of the different incubation times are indistinguishable, as also seen by the black symbols in Figs. 7C–H, indicating averages of histogram ratios for up to 100 pairs of all combinations between the studied 3D images. However, such analyses clearly show higher proportions of longer $F_1\boldsymbol{\alpha}$ inter-distances in the 3D images of hypoxic samples relative to normoxic samples or those with dm2OG. In detail, an up to 60% increase is indicated in the appearance of longer 70–140 nm inter-distances between $F_1\alpha$ antibodies at hypoxia compensated by an up to 40% decrease in the appearance of inter-distances < 70 nm (Fig. 7C,D). A restoration of nearly original cristae morphology and/or width upon the addition of dm2OG to hypoxic HepG2 cells is indicated by similar patterns for the hypoxic samples normalized to dm2OG samples (Fig. 7E,F). A support comes also from an average normalization of dm2OG to normoxic samples declining from plus to minus 5% and 10% for increasing inter-distances of samples with a 10-min and 2-h incubation, respectively (Fig. 7G,H). An analysis of dm2OG at normoxia is shown in Supplemental information (Fig. S1B).

3.5. Apparent presence of multiple ATP-synthase oligomers in normoxic or dm2OG-treated cells reflects higher stability of ATP-synthase dimeric rows compared to hypoxic cells

BN-PAGE separating protein complexes from lysates of glycolytic HepG2 cells (in a medium either with 5 mM or 25 mM glucose, "Glc") or galactose/glutamine-metabolizing HepG2 cells ("OXPHOS", forced to oxidative phosphorylation) exhibited a higher hexamer and tetramer proportion for normoxic samples, when compared to the hypoxic samples (Fig. 8, Fig. 9). This is compared vs. the entire ATP-synthase content in the corresponding Western blots with $F_1\boldsymbol{\alpha}$ antibodies. Samples of hypoxia-adapted cells incubated for 30 min or 5 h with dm2OG exhibited nearly the same oligomer-to-entire-content ratios as the normoxic samples (Fig. 8, Fig. 9, Fig. S2).

To interpret these results, we elaborated a hypothesis (see Discussion), outlined in Fig. 10. Our hypothesis expects the existence of labile ATP-synthase dimeric rows associated with the wider crista and longer inter-rim distance, and conversion to the narrower crista and shorter inter-rim distance upon strengthening the ATP-synthase rows of dimers. More labile rows should form much fewer tetramers and higher oligomers after the same solubilizing procedure, when compared to the more stable rows of normoxic samples and hypoxic samples with dm2OG. We hypothesize that the lower cross-linking along the longitudinal crista rim axis, forming a flatter rim and hence only being able to hold a wider crista, can be transferred into the high (saturated) cross-linking of dimers within the row. The maximum cross-linking should be ordering this row, so that the ability of ATP-synthase to bend the membrane will form the sharpest rim. As a result, this sharpest crista edge will hold the narrowest possible crista lamella (Fig. 10, bottom scheme), when the lipid and protein complexes are conserved during the transition. The unconnected dimers are allowed to transversally fluctuate, and consequently cannot sharpen the membrane. The resulting membrane is flatter and the width and/or inter-rim distances are larger (Fig. 10).

3.6. Distinct relocations of mitofilin and SAMM50 reflect disconnection of MICOS-SAM complexes in hypoxia and their re-assembly upon increasing substrate load

Next, we employed double-color 3D dSTORM for simultaneous imaging of SAMM50 subunits of the SAM/TOB complex in the OMM and mitofilin/Mic60 within the IBM. Since mitofilin is the major component of the MICOS complex, the proximity of SAM and mitofilin markers (given by overlays of their 3D images) indicates locations of these MICOS complexes (Fig. 11). We have confirmed the previous observation in normoxia [1] that mitofilin/Mic60 is isotropically spread throughout the approximately cylindrical surface of the IBM (Fig. 11; Fig. S3). Note that the IBM forms the inner "cylinder" inside the OMM. Obviously, the OMM is composed of nearly cylindrical mitochondrial network tubules [1]. In contrast now, Fig. 11 shows that the sparse SAMM50 spots were located in clusters. We may expect these clusters to indicate the positions of MICOS complexes (Fig. 11). Besides the cluster analysis, here we also employed calculations of a number of the projected mitofilin/Mic60 localizations into the modeled IBM. The IBM was modeled using the Auto Skeleton algorithm of the software Amira 5.5 and then the surface of the resulting tubules at each given segment was calculated. Next the point density (a number of localization *per* unit of surface area) was calculated. Note that these calculations were consistent with the analyses of histograms derived from the 3D Ripley's *K*-function.

We also noticed that the positions of crista junctions (outlets) presumably formed by the surrounded MICOS complexes are readily recognized in FIB/SEM images. In the tested OMM segments they appeared to be randomly distributed vs. the cylindrical OMM surface

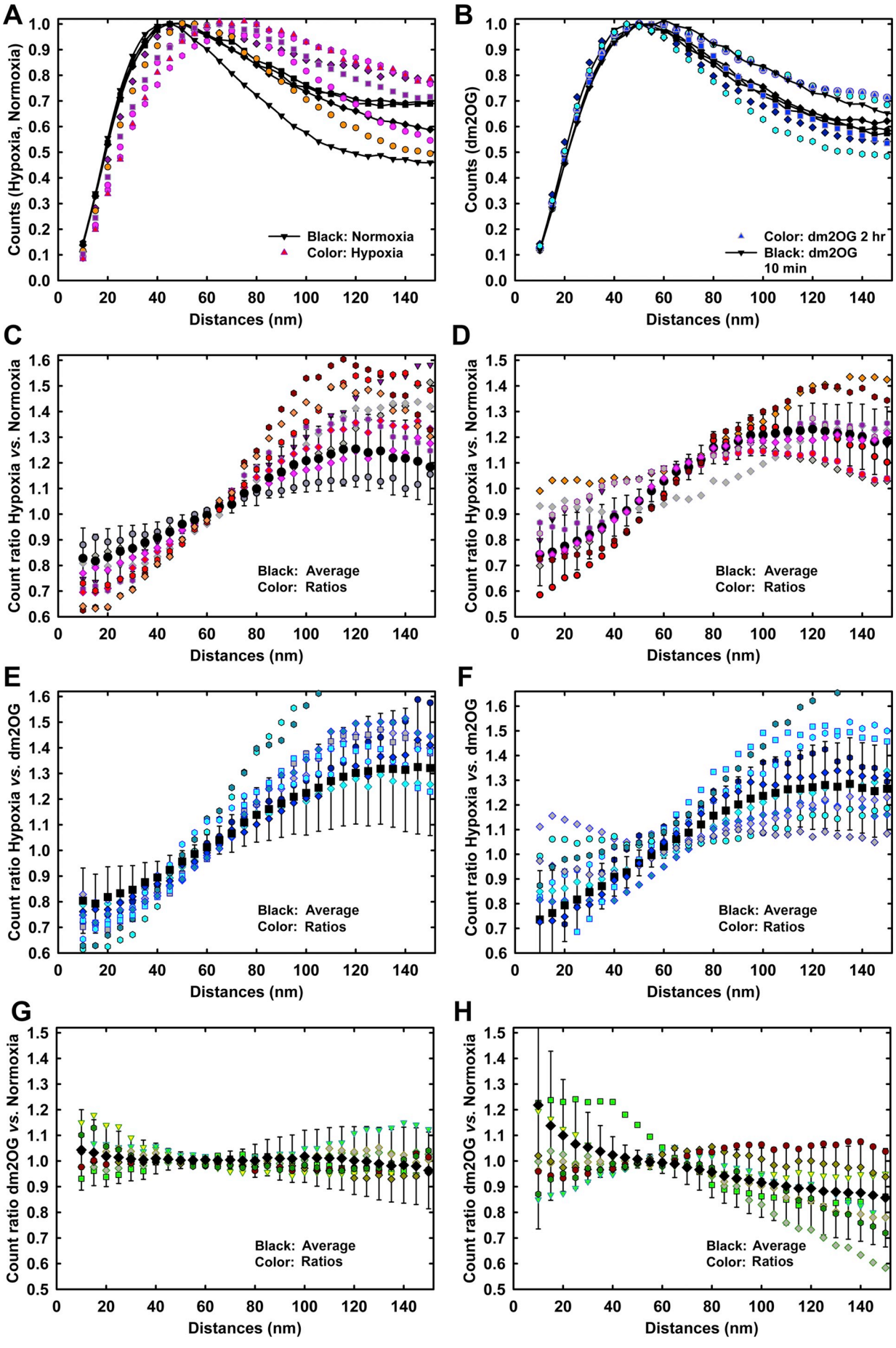

(caption on next page)

Fig. 7. Comparison of histograms for 3D inter-distances between $F_1\alpha$ subunits of ATP-synthase.
All panels show the calculated ratios between the two corresponding histograms for the 3D inter-distances of the primary antibodies (anti-α-F_1-sector subunit of the ATP-synthase, $F_1\alpha$) from up to 100 pairs (combinations) of 9–12 studied 3D dSTORM images for each condition. The Ripley's K-function of 3D stochastic super-resolution microscopy data was transferred to histograms by the procedure briefly described in Methods and published elsewhere [41].
A) Examples of several histograms for 3D images of normoxic (*black symbols plus lines*), hypoxic (*all shades of pink*, *magenta*, *violet*, *orange*), and **B**) comparison of normoxic to hypoxia-adapted cells incubated with dm2OG for 10 min (*black symbols plus lines*) or 2 h (*all shades of blue*).
C–H) Example ratios between histograms for the indicated samples and averages of the entire existing ensemble of combinations (*black* points with SDs). Color code: C, D) hypoxic vs. normoxic samples (*all shades of gray*, *pink*, *magenta*, *violet*, *orange*); E, F) hypoxic vs. hypoxia-adapted and incubated with dm2OG (*all shades of gray or blue*); and G, H) hypoxic with dm2OG vs. normoxic samples (*all shades of gray or green*).

(Fig. 4). Note also that a large fraction of „free "mitofilin/Mic60 molecules exists, which is not connected to the SAM complex (Fig. 11). We cannot currently distinguish whether these mitofilin/Mic60 subunits are assembled in immature MICOS complexes or exist as monomers. We also confirmed [1] that mitofilin/Mic60 molecules clustered upon hypoxia into larger clusters than SAMM50 does, whereas the pattern of SAMM50 remained quite similar (Fig. 11). Previously, we reported that upon hypoxia overall ~20% of the mitofilin/Mic60 is degraded [1]. This can also be seen in Fig. 11D, G, and Fig. S3. The resulting partial MICOS detachment from the OMM SAM contacts allows free MICOS lacking Mic60 to expand the crista outlets (crista junctions) [1].

Upon hypoxia, MICOS clusters are formed (analyzed in Fig. 12), since the inflated cristae lamellae at hypoxia should nearly touch each other [1] and since the crista outlets bear the MICOS complex containing Mic60. As a result, the Mic60 molecules from the two neighboring and very close enlarged crista outlets also come very close to each other (Fig. 13A).

We then examined samples in which dm2OG was added to hypoxia-adapted HepG2 cells for 10 min or 2 h. If a simple reversal of hypoxic cristae widening process occurred, the Mic60/mitofilin should disperse the clusters formed in hypoxia. Indeed, upon the addition of dm2OG to hypoxia-adapted HepG2 cells, decays of Mic60/mitofilin clusters were then observed, in contrast to the previously established clusters upon hypoxia (green color in Fig. 11E,H vs. D,G; cf. Fig. 11C,F for normoxia). With dm2OG, the Mic60/mitofilin became more random (cloudy) in the corresponding super-resolution 3D images (Fig. 11E,H), as judged from projections to the modeled IBM (Fig. 12A). These results are consistent with the narrowing of the crista outlets (junctions) concomitant to the cristae narrowing.

Note that the clustering means decreased inter-distances (that are not always the most frequent). Hence, a decrease in MFD for the Mic60 3D dSTORM images upon hypoxia could be expected. Indeed, the histograms of 3D inter-distances between the secondary antibodies recognizing anti-Mic60 antibodies gave a shorter MFD, when compared to

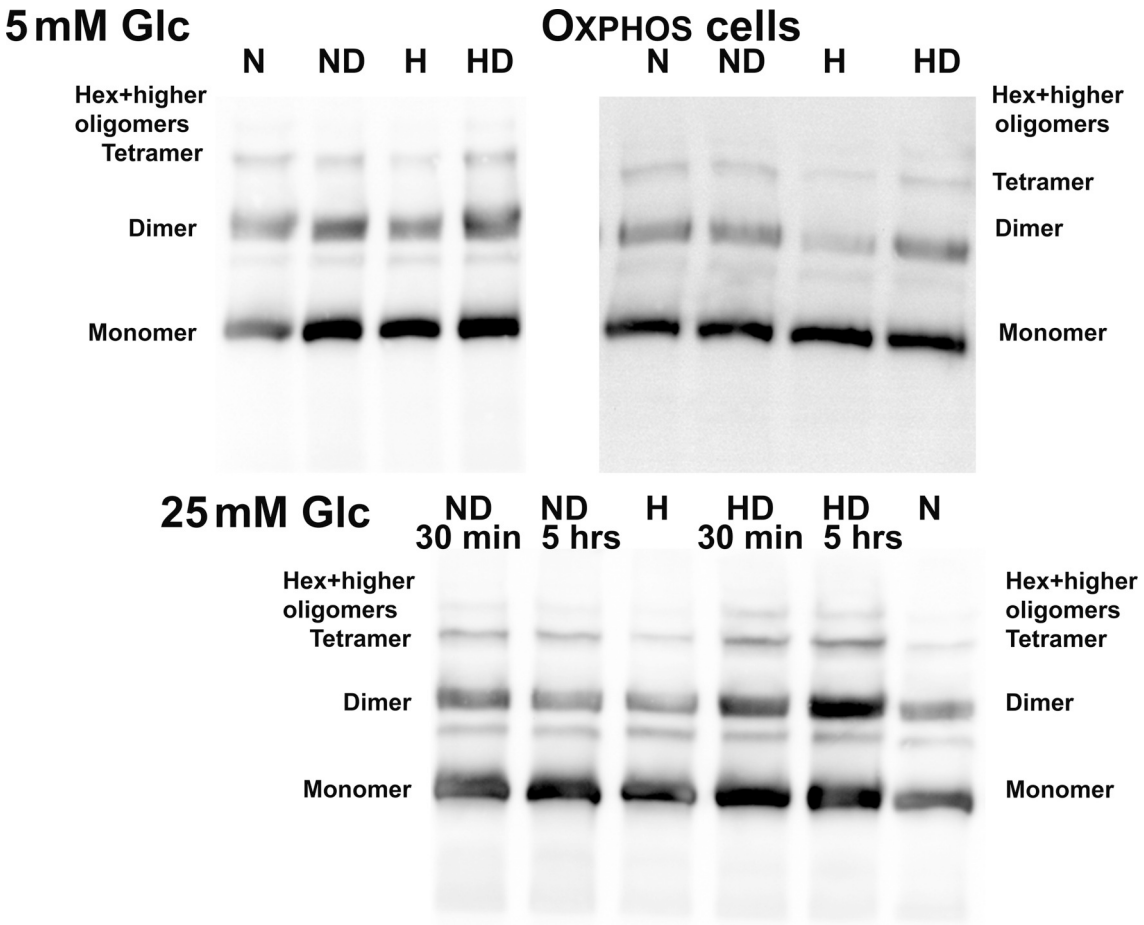

Fig. 8. BN PAGE: Recruitment of novel ATP-synthase dimers and higher oligomers upon increasing substrate load.
Western blots stained for $F_1\alpha$ are shown for the BN PAGE of lysates from HepG2 cells cultured in media with 5 mM glucose ("Glc"), 25 mM glucose or galactose ("OXPHOS cells") as indicated at normoxia ("N"), 5% O_2 hypoxia for 72 h ("H"), after 30-min or 5-h subsequent incubation with 4 mM dm2OG for hypoxia-adapted cells ("HD"), or after incubations with 4 mM dm2OG at normoxia ("ND").

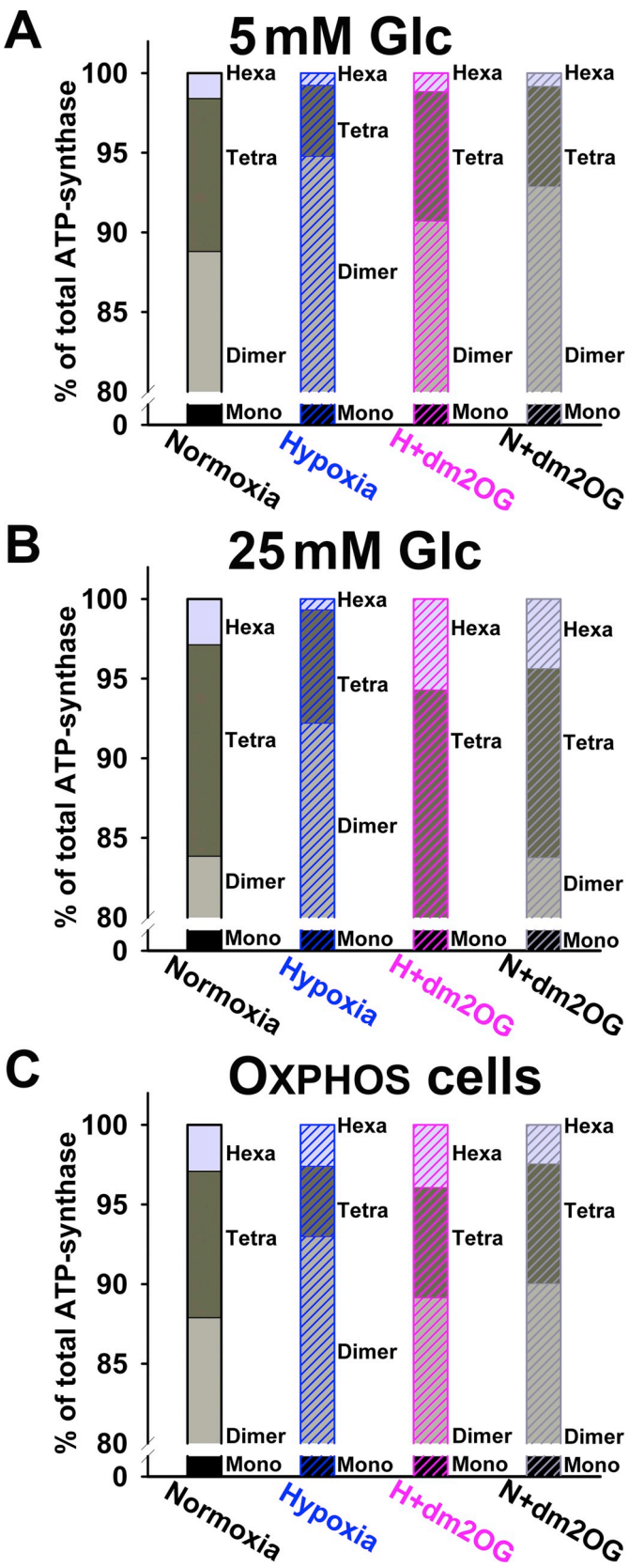

Fig. 9. Quantification of hexamer/higher oligomer portion and tetramer portion vs. entire ATP-synthase content.
Quantification emphasizing tetramers and hexamers of ATP-synthase was performed from Western blots such as shown in Fig. 8 for each studied situation as indicated. "H" hypoxia, "N" normoxia; "Hexa", hexamers plus higher oligomers; "Tetra", tetramers; "Mono", monomers. For precise quantification of dimers and monomers see Fig. S2.

the dm2OG hypoxic treatment; and even shorter than those for normoxia (Fig. 12C). A high fraction of short inter-distances between the Mic60/mitofilin molecules at hypoxia can be recognized (Fig. 12E); as well as its decline after the addition of dm2OG. The latter indicates the even spreading of Mic60/mitofilin molecules (Fig. 12E), similar to normoxia (Fig. 12G, blue points). The latter transition reflects the narrowing of crista outlets, as shown in Fig. 13A. Notably, the range of higher inter-distances was increased after the addition of dm2OG to normoxic cells (Fig. 12G, gray points).

Interestingly, upon high dm2OG load, the OMM complex SAM behaved in a different way (red color in Fig. 11E, G vs. D, H; cf. also Fig. 11C, F for normoxia; and Fig. 12B, D, F, H). Despite the fact that the surface density of the SAMM50 component of SAM also somewhat increased (Fig. 12B), the calculated MFD did not change (Fig. 12D,F). Perhaps the density calculated towards the modeled IBM, which changes at a constant OMM diameter [1] may explain this inconsistency. Nevertheless, no significant change in MFD for SAMM50 after the dm2OG load is consistent with the detachment of SAM complexes from MICOS at hypoxia. The absence of SAMM50 relocation causes SAMM50 to appear to have a similar pattern with regard to MFDs (Fig. 12D,F). The latter occurs because the SAM complexes which are detached from the MICOS complexes remain in approximately their original positions. However, there was a statistically significant increase in MFD for SAMM50 in hypoxia vs. normoxia (Fig. 12D). Despite the fact that the SAM clusters remain in the OMM in hypoxia, the distances reflecting these clusters which contribute predominantly to the ensemble of inter-distances for the normoxic samples now cannot dominate in hypoxia, also due to some fraction of the detached SAM from crista junctions (Fig. 13B). However, if SAM relocations exist, they should be studied further.

3.7. Validation of method deriving inter-distance histograms from the 3D Ripley's K-function to reflect 10-nm shifts in distances between objects

We also demonstrated the ability of our method to reflect 10-nm shifts in the distances between two planes or objects. Our simulations (Fig. 14) show that if the real distance is enlarged by 10 (20–50) nm, the resulting MFDs also approximately increase by this increment. Nevertheless, this method cannot be used as a precise ruler for the reason given below.

The acquisition of 3D dSTORM images can be obscured by a different antibody staining density [53] and a higher fraction of background signal. We therefore tested the simulations of 3D clusters of points at different signal densities and shapes (see online Supplemental Information Figs. S4–S7) and calculated the resulting 3D Ripley's *K*-function according to Eq. (2), using the software Vutara. From the resulting *K*-functions, we derived the histograms with a step of 5 nm for all possible inter-distances between the simulated points. Our simulations showed that the size of clusters decreases the magnitude of MFD, but does not prevent cluster recognition.

In order to model situations similar to our experimental 3D dSTORM images of $F_1\alpha$ ATP-synthase immunocytochemistry, we simulated small symmetrical clusters of points with a full width at a half-maximum (FWHM) of 10 nm, which were randomly positioned inside the 20-nm thick parallel planes. These planes were also parallel to the xy-plane. The considered space was limited to only 2 μm × 2 μm × 50 nm (x × y × z). Next, we varied the distance between the centers of these two planes from 50 nm to 100 nm (Fig. 14A) and calculated the 3D Ripley's *K*-function, from which we derived the corresponding histograms of inter-distances between the simulated points. In all cases, we plotted histograms for each plane separately and compared this to the entire 3D image (Fig. 14B–F, all panels "a"). We also subtracted histograms for both planes alone from the histogram of the entire 3D image, yielding a histogram reflecting the net inter-distances between the two modeled planes (Fig. 14B–F, all panels "b").

As a result, in all cases we obtained MFDs very close to the real

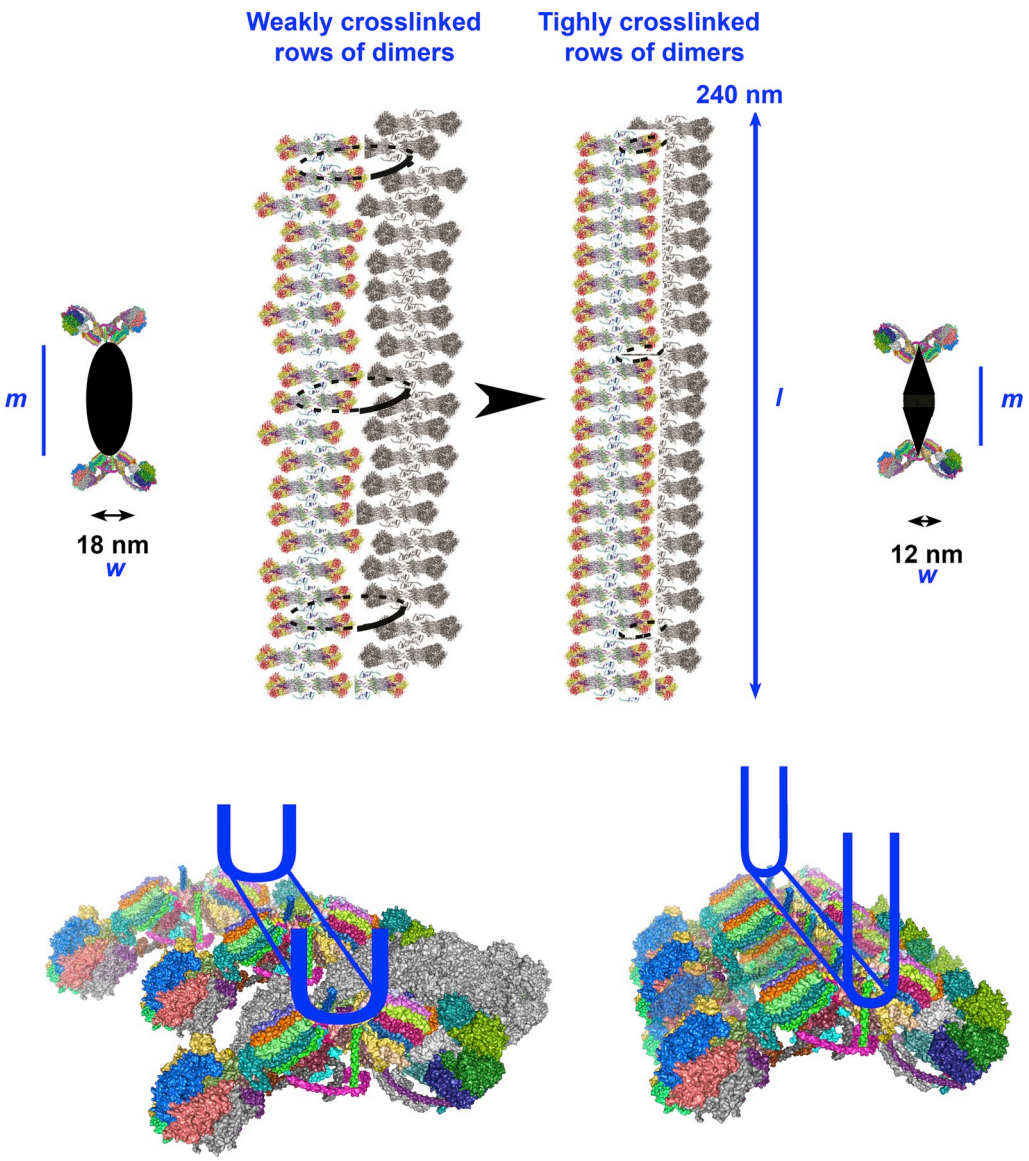

Fig. 10. Hypothesis illustration.
Top schemes in the center show the crista from the nearly front view in relation to the sharp rim (edge). The crista cross-sections are depicted by the ellipses (having *w* and *m* axes). The central illustrations are surrounded with crista cross-sections (*black*) shown as the top-views of the crista through the crista outlet. *Bottom schemes* show the octamers of the ATP-synthase modeled as described in the Legend to Fig. 6E. The ICS (IMM) membrane, showing the narrower crista profile *w*, is drawn in *blue*. Two situations are depicted: *Left*: wider cristae with weakly cross-linked rows of ATP-synthase dimers; *Right*: narrow cristae with tightly cross-linked rows. The width of the ATP-synthase dimer is taken from references [29, 58] as modeled in Fig. 6E.

geometrical distances between the centers of the two planes. Thus for a series of double parallel planes with their centers 50–100 nm apart with a step of 10 nm, MFDs of 65, 75, 80, 100 and 115 nm, respectively were obtained from those differential histograms (Fig. 14B–F, all panels "**b**"). MFDs for histograms of the entire 3D images for this series were equal to the previous values with the exception of the 60 nm distance between the planes (Fig. 14B–F, all panels "**a**"). In that instance, the fluctuation is just equal to the step in the histogram.

These simulations show that if the real distance is enlarged by 10 (20–50) nm, the resulting MFDs also approximately increase by this increment. Therefore, we demonstrated the ability of our method to derive the inter-distance histograms from the 3D Ripley's *K*-function to reflect 10-nm shifts in distances between objects. In conclusion, our simulations of planes composed of clusters provided results confirming that any local maximum can appear in the histogram, in which such a local maximum represents the approximate distance between the two layers (despite the fact that tilted inter-distances may predominate). To simulate the complex topology of mitochondrial cristae, more adequate modeling would require breaking these planes into numerous patches randomly oriented within the space. Nevertheless, our method is robust enough to recognize changes in MFD under different experimental conditions. However, this method cannot be used as a precise ruler because of the obvious presence of proximal but tilted inter-distances between the theoretical planes that might be used for the measurement.

4. Discussion

In this work, we documented that mitochondrial cristae morphology reflects the metabolic demands of cells even within short time periods of ~10 min. A sudden increase in the respiratory substrate load (2-hydroxy load) led to the narrowing of already hypoxia-widened cristae in glycolytic hepatocellular carcinoma HepG2 cells. This finding might represent a prototypic example of cases in which the in vivo cristae morphology reflects the intensity of OXPHOS [3,4]. The resulting changes could also establish a more efficient bioenergetics state [54]. One may speculate that mitochondrial cristae may change their width and inter-rim distances, hence altering their morphology, during a very short period. We may predict that the physiological widening of cristae proceeds upon a substrate shortage, whereas the opposite process of physiological narrowing is induced by an excess of the respiratory substrate. Our sudden addition of 2dmOG only represents such an excess of 2-oxoglutarate. Moreover, a similar cristae narrowing was found with the increasing glucose metabolism in pancreatic β-cells, i.e. at the transition when the insulin secretion is stimulated [43]. The previously reported hypoxic cristae widening in parallel to crista junction (outlet) widening also indicated that cristae did not have a "balloon "shape.

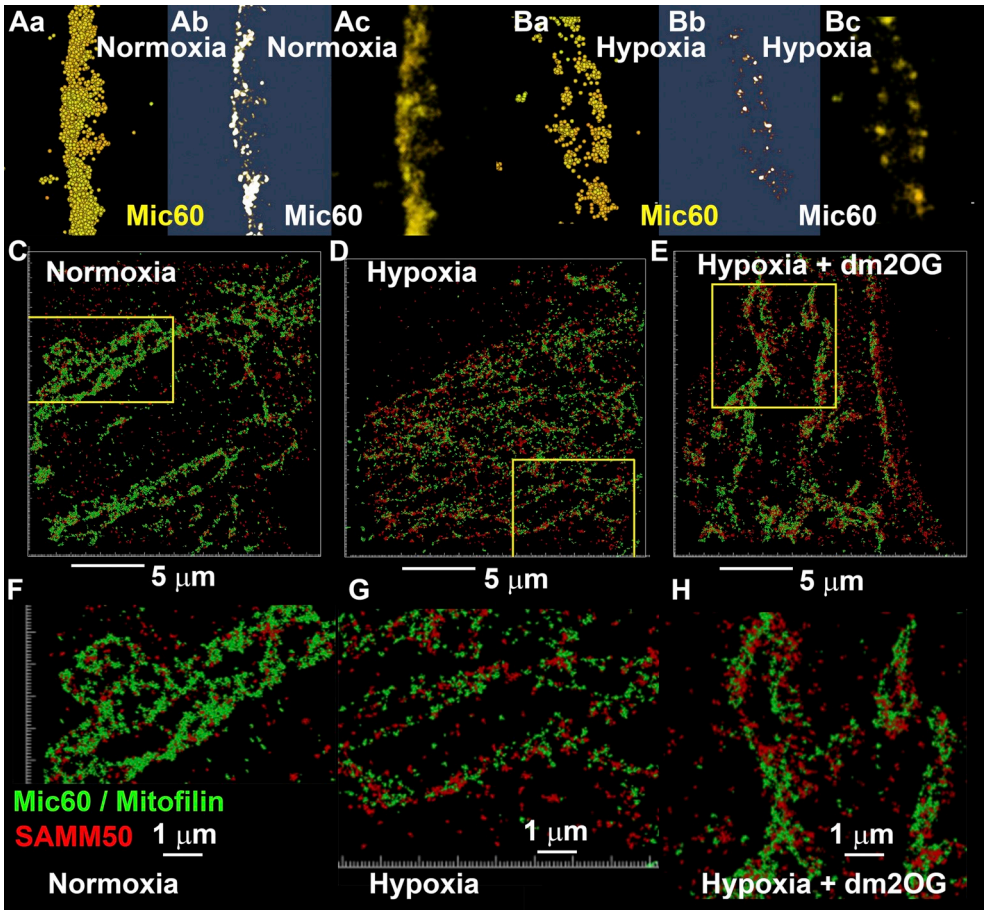

Fig. 11. High substrate dm2OG load on hypoxia-adapted HepG2 cells – changes in Mic60/mitofilin and SAM distribution.
Single Mic60/mitofilin (Aa–Ac, Ba–Bc) and double-color (C-H) dSTORM 3D image projections for simultaneous imaging of the SAMM50 subunit of the OMM complex SAM/TOB (*red*) and Mic60/mitofilin (*green*) in the IMM.
A, B) Hypoxia-induced Mic60/mitofilin clustering (B) as compared to normoxia (A). Subpanels a, b, c depict spherical, smoothed, and point-splatting image representations, respectively.
C–H) dm2OG effect on hypoxia-adapted HepG2 cells (F-H are zoomed from yellow framed areas of panels C–E): C, F) normoxia; D, G) hypoxia; E, H) incubation of hypoxia-adapted cells with 4 mM dm2OG for 2 h. Hypoxic adaptation took over 72 h at 5% O_2.

This is also largely excluded by the acquired FIB/SEM images showing the nearly parallel crista lamellae having only small outlets to IBM (crista junctions with OMM). Also, during the opposite process of cristae narrowing the cristae lamellae as well as crista junctions decrease their size in parallel.

Due to its speed, the acute mechanism behind cristae morphology changes cannot be due to a protein expression. Hence, any transcription up-regulation can be excluded, at least for 10-min incubations with dm2OG. Nevertheless, fast *post*-translational modifications of certain cristae-shaping proteins might be involved. Isovolumetric morphology changes of cristae lamellae were suggested by good fits of the aspect ratio dependences on the cristae width (Fig. 3E,F) for such an isovolumetric model (Fig. 3G), which is consistent with the absence of protein and lipid synthesis. We have to analyze the behavior of the two major components that determine the cristae architecture and morphology. These are the rows of ATP-synthase dimers along the crista rims and MICOS complexes at the crista outlets. MICOS joins the OMM SAM/TOB complex, thus forming so-called crista junctions.

We have previously found that the hypoxic widening of cristae is accompanied by the shortening of the cristae length (the distance of the crista end from its outlet) [1]. When the reverse phenomenon occurs, i.e., cristae narrowing, it can be seen that the shorter and bulkier hypoxic cristae (Fig. 2, panels a) lengthen with dm2OG (Fig. 2, panels b). Their aspect ratios are a good fit to our model of 3D crista lamellae (Fig. 3D), which predicts a reciprocal quadratic dependence on the crista width. These data support the possibility that the process does not require de novo lipid synthesis or lipid recruitment to build-up a new membrane.

Our 3D dSTORM data are not saturated in terms of bound antibody at each $F_1\alpha$ subunit [53]. We can speculate that our data only contain a few fluorophore localizations *per* a single crista. This is recognized at high magnification and with the inspection of 3D images (Fig. 6 Ac, d and cf. Fig. 5 in Ref. [43]). That is why the 3D dSTORM data provide useful statistics that automatically obtain numerous estimates. We have to do this without precise knowledge of the distance representing the derived MFD, which may originate from a mix of the inter-rim distances and their tilted representations with the “top of V” distances within a single monomer. The ensemble of inter-distances undoubtedly involves the inter-cristal distance of ~90 nm (mean distance between the neighbor crista junctions) as well. However, on the basis of a realistic 3D model of crista (Fig. 3G, 6C,E), we can predict that the MFD for the $F_1\alpha$ subunits determined by 3D dSTORM most likely represents the distance between the two opposite cristae rims, i.e. ICS membrane ridges, termed the inter-rim distance (“*m*” in a Fig. 3G, an intermediate from the three dimensions of the cuboid model). A lower contribution to the ensemble may be made by the “top of the V” distance, i.e. the inter-F_1-moiety distance within a single ATP-synthase dimer. The latter is however quite unlikely, since the simultaneous antibody staining of both monomers within a single ATP-synthase dimer is rare. In conclusion, we cannot use MFD as a precise ruler. However, as we show in the Chapter 3.7 (Fig. 14 and Appendix I in the online Supplementary material) using theoretical modeling, the method is robust enough to be able to detect in the geometrical distances at a nm scale.

Distances derived from the 3D dSTORM data are isotropic, i.e. are independent of the angle of tubular or spheroid sections, unlike TEM images. Note also that the TEM sections which are precisely perpendicular to the longitudinal tubule axis cannot show any apparent crista when the actual crista is precisely perpendicularly oriented. We do not deny the usefulness of FIB/SEM tomography, however obtaining appropriate statistics by FIB/SEM is very demanding in terms of acquisition time and cost. The ideal imaging approach would be to perform a 3D super-resolution fluorescence microscopy correlated with FIB/SEM

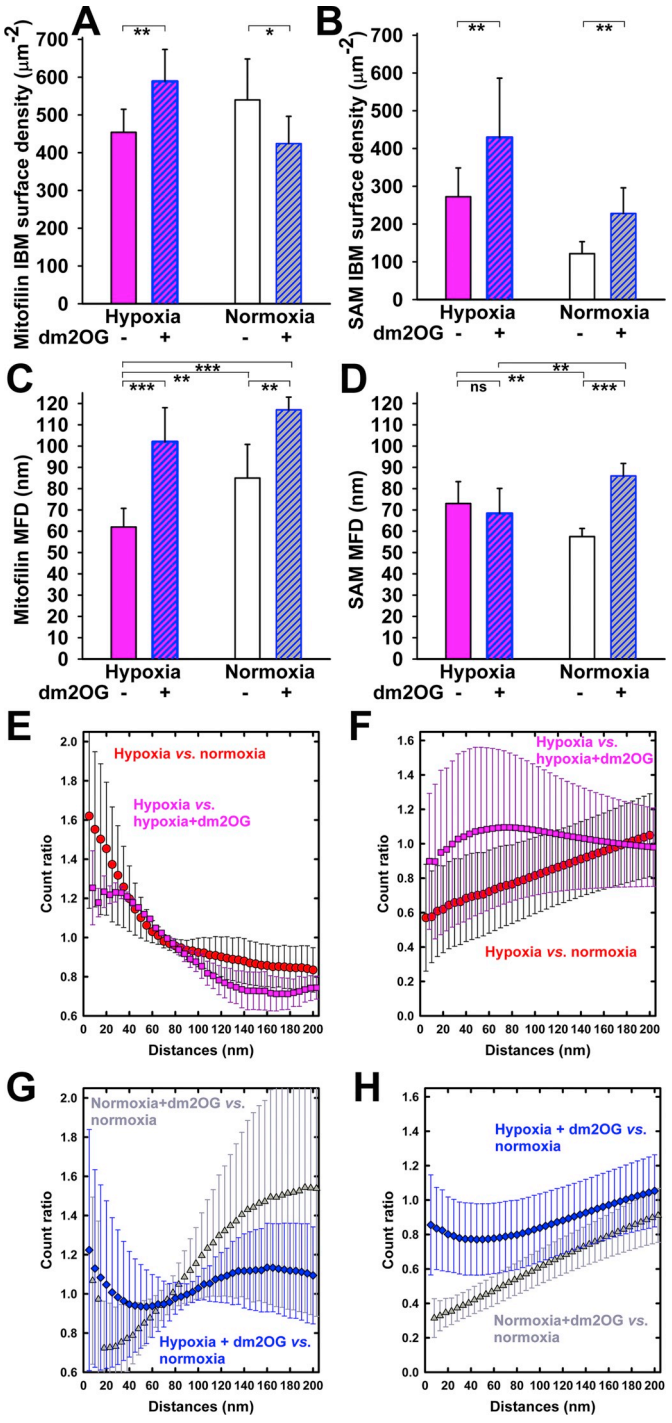

Fig. 12. Analyses of 3D double-color dSTORM images of Mic60/mitofilin and SAM distribution.

Where indicated, hypoxic adaptation took over 72 h at 5% O_2 or subsequent incubation with 4 mM dm2OG lasted 2 h. Data are taken from the ensemble of 3D images such as illustrated in Fig. 7C–E).

A, B) Localized point densities expressed as projections to model cylinder approximating OMM for Mic60/mitofilin (A) and SAM/Samm50 (B). C—H) Analyses of histograms derived from Ripley's K-function for Mic60/mitofilin (C, E, G) and SAM/Samm50 (D, F, H) yielded the resulting MFDs (C, D) and averages of ratios between histograms for the indicated samples within the entire existing ensemble of combinations (E–H) between 5 and 10 images for each group. Color code: hypoxic vs. normoxic samples (*red*); hypoxic samples vs. hypoxia-adapted and incubated with dm2OG (*magenta*); hypoxic dm2OG vs. normoxic samples (*blue*); and normoxic vs. normoxic incubations with dm2OG (*gray*).

or other electron microscopy tomography. Such a promising approach will enable us to understand mitochondrial cristae topology and its changes due to metabolic demands.

Moreover, on the basis of BN-PAGE results, we derived the evidence supporting the essential role of the ATP-synthase dimeric rows in the mediation of cristae width changes [55]. Without exceptions, we always observed a correlation of a less abundant appearance of the ATP-synthase tetramers or hexamers plus higher oligomers with the existence of wider cristae width; and vice versa, a higher oligomer appearance in Western blots of BN-PAGE from the normoxic cells [1]. In this work, the latter was also observed for hypoxia-adapted cells upon high 2-oxoglutarate (dm2OG) substrate load.

Since ATP-synthase monomers only exist in the IBM, whereas ICS membranes only contain ATP-synthase dimers [56], the morphology of cristae cannot be governed by the ATP-synthase dimeric fraction, but by the stabilization/destabilization of the existing rows of dimers along the sharp cristae rims. In fact, the dimeric fraction (including dimers within the higher oligomers) should always be close to 100%, when ignoring presumed assembly intermediates. We interpret the disappearance of tetramers, hexamers or higher oligomers on the resulting BN-PAGE Western blots as a result of more labile rows of ATP-synthase dimers existing in vivo. It is simply the case that the equal solubilization procedure disrupted more of them for the labile samples (hypoxic in our case). In contrast, the solubilization left more remnants of the original rows as dimers or even tetramers or hexamers. These less labile, hence stabilized, ATP-synthase rows were thus indicated for normoxic cells and hypoxia-adapted cells after the higher substrate load.

Fig. 10 illustrates our hypothesis, describing the mechanism of conversion of the labile ATP-synthase dimeric row into wider crista; or vice versa, the conversion into narrower cristae upon strengthening the ATP-synthase row of dimers. We predict the following process: *i*) when a lower stabilization or partial cross-linking (by certain small proteins, such as Mic10 [35–37] or DAPIT [30–34]) exists within the row of ATP-synthase dimers [29], such labile rows allow their dimers to fluctuate perpendicularly to the original longitudinal rim axis. The membrane is then curved not in a synergy along a single line, but randomly, probably in a zig-zag line, in certain parts of the rim. These random fluctuations of dimers are predicted to flatten the originally sharp bending of the membrane (Fig. 10, left part). As a result, the flattened edge allows the inflation of the crista along its long and medium (inter-rim *m*) dimension and, therefore, an increase in its width *w*. With longer periods enabling de novo biogenesis, the ICS volume may also increase.

In contrast, *ii*) nearly completely, and hence tightly, stabilized and/or cross-linked rows of ATP-synthase dimers along the crista rims must form the sharpest crista edges, reaching the smallest angle (Fig. 10, right part) [28]. Note that this angle is determined by the dimeric ATP-synthase architecture and even by the shape of the monomeric F_O-ATPase [28,29,57–60]. This takes place in synergy with the MICOS and specifically with the Mic60 subunit [12] and with the protein OPA1 [5]. Thus the MICOS complex sets the narrowest crista outlets under these conditions (see below), and therefore such cristae reach the narrowest morphology.

An earlier work reported on the narrowing of cristae after starvation [5]. A concomitant autophagy causing losses of membrane may explain this situation in which the opposite cristae behavior was reported. So then the lack of widening would be prevented by insufficient membrane components to form wider cristae. Also, fatty acid oxidation at starvation may represent a higher substrate load, so if this existed, the reported results are in accordance with our report on HepG2 cells.

Synchronization of the two should exist since the cristae lamellae do not exhibit a “balloon” shape. Ongoing morphology changes affect crista junctions (outlets) on one hand, and the crista edges on the other [1,3,7]. Most likely there is recruitment for the MICOS-bound Mic60/mitofilin from a pool of free Mic60/mitofilin molecules (see Fig. 11C–H) into the newly assembled MICOS upon high substrate load. The recruited and re-assembled MICOS subsequently joins the OMM

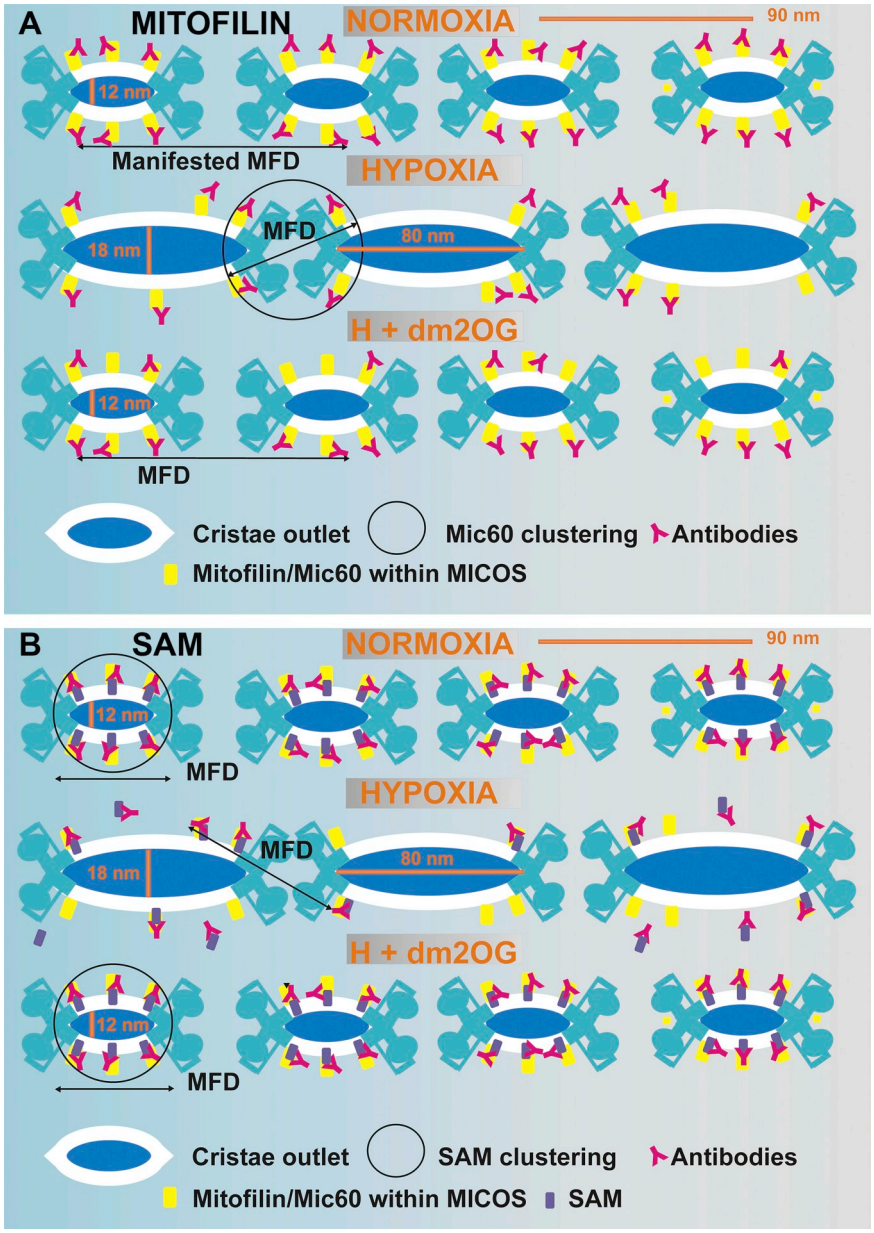

Fig. 13. Interpretation of inter-distances histograms for Mic60/mitofilin and SAM.
A) Mic60/mitofilin; B) SAM. Schemes depict the crista junctions (outlets) viewed from the top (i.e., perpendicularly to the OMM plane with projections of the ATP-synthase dimers (*blue-green*) and MICOS complexes (*yellow*) or SAM complexes (*purple*) containing anti-Mic60 or anti-Samm50 antibodies (both *red Y*). At normoxia, experimental data yielded the derived MFDs in accordance with the Mic60 inter-distances of the neighboring crista outlets. In contrast, upon hypoxic clustering due to intracristal space inflation (cristae width depicted as increasing in a single direction), MFDs reflect Mic60 inter-distances between "cluster surfaces". The high substrate (dm2OG) load reverses the hypoxic conformation.
The manifested MFDs for SAM imaging are obtained from the SAM inter-distances between the neighboring crista outlets. However, since a portion of SAM molecules are detached from Mic60/mitofilin, as well as the MICOS complex of IMM at hypoxia [2], the corresponding SAM MFDs increase at hypoxia. The high substrate (dm2OG) load reverses this hypoxic conformation.

SAM/TOB complexes. This might explain the mechanism of cristae narrowing in the vicinity of crista outlets (junctions with OMM). This interpretation best matches the Mic60 and SAMM50 relocations observed by double-color 3D super-resolution microscopy. Also, when arrays of crista outlets exist preferentially on opposite sides of the cylindrical mitochondrial tubules, the crista outlet projection may then appear as two parallel lines, especially when there is a dense coverage of Mic60 by fluorophores [11].

Our previously revealed mechanism [1] of hypoxic cristae widening was partly HIF-independent, occurring in two phases: a fast phase involving both the detachment of MICOS-SAM contacts plus destabilization of ATP-synthase rows along the crista rims; and the second phase which is a delayed HIF-dependent phase, further intensifying the detachment of MICOS-SAM contacts by the HIF-mediated degradation of Mic60/mitofilin, Mic10 and possibly other MICOS components [1].

Proton pumps of respiratory chain complexes I, III, and IV use the redox potential of electron transfer to pump protons from the matrix space to the ICS and thus create the protonmotive force Δp. A compartmentalized proton coupling then occurs within the ICS [2,23]. As a result, any changes in the shape and volume of the ICS affect the coupling efficiency between the Δp established across the ICS part of the IMM and the proton backflow through the ATP-synthase F_O sector back to the matrix [2,54]. Also, the formation of superoxide, H_2O_2 and other reactive oxygen species (ROS) by mitochondria and subsequent redox regulations should be related to cristae morphology and vice versa [2]. We have predicted that cristae morphology changes significantly participate in retrograde redox signaling from mitochondria [2].

5. Conclusions

We have demonstrated cristae narrowing with a high substrate load on hypoxia-adapted HepG2 cells. This followed the previous findings of hypoxia-induced cristae widening in these cells. Cristae narrowing, proceeding even within a very short period, is most likely determined by the strengthening of the ATP-synthase dimeric rows at the cristae rims. This was accompanied by the relocation of proteins joining the inner and outer membranes at so-called contact sites, specifically by relocating the Mic60 subunit of the MICOS complex and re-joining it to the SAMM50 subunit of the SAM/TOB complex.

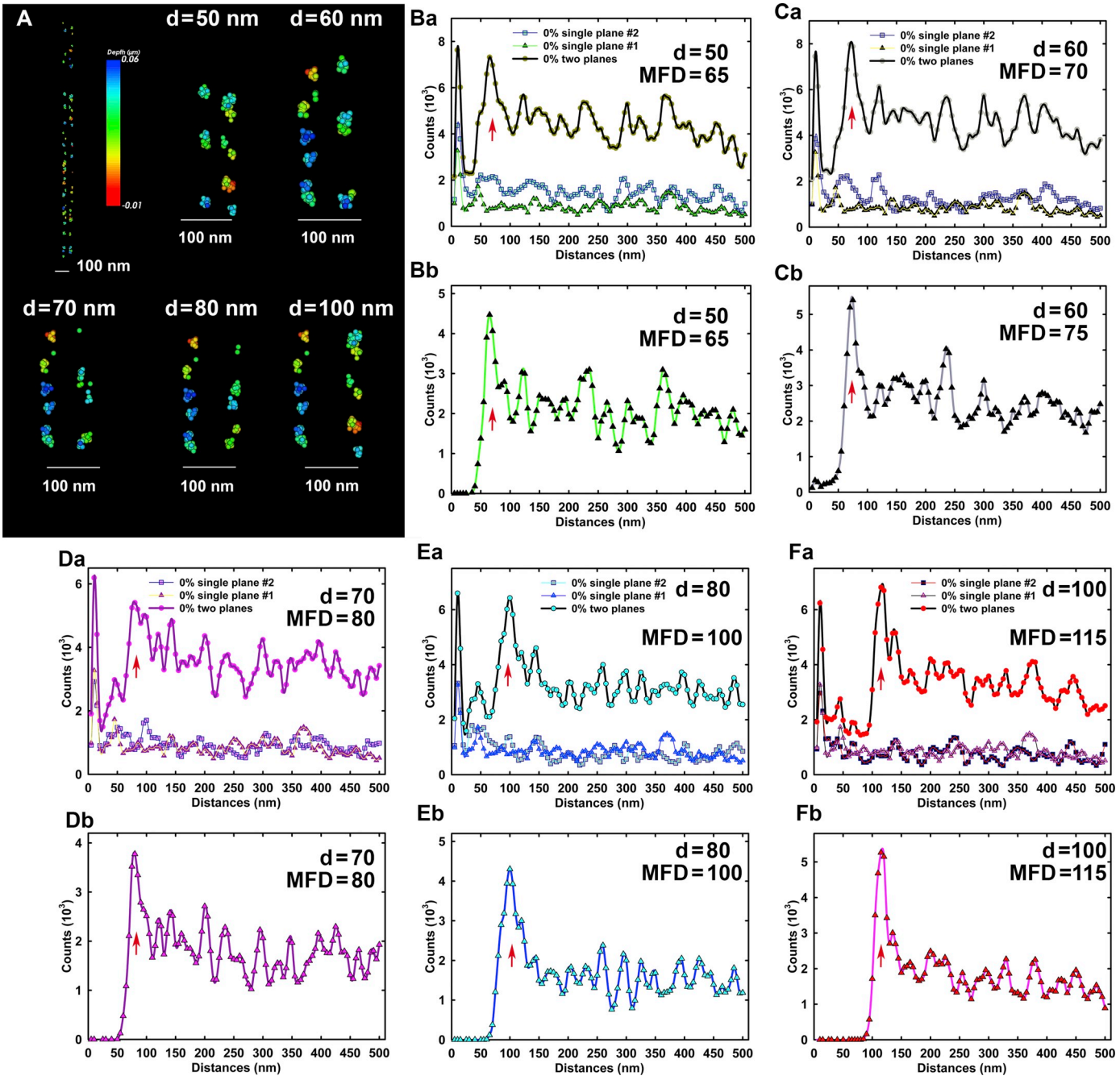

Fig. 14. Variation of most frequent distances (MFD) with increasing distance between parallel planes.
A) Simulated 3D images were constructed by random positioning of small symmetrical clusters of points, with a full width at half-maximum (FWHM) of 10 nm, inside the 20-nm thick parallel planes. These planes were also parallel to the xy-plane inside the 2 μm × 2 μm × 50 nm (x × y × z) space. Distances d between the centers of planes were set from 50 nm to 100 nm as indicated.
C–H) The resulting histograms of inter-distances between the simulated points as calculated from the 3D Ripley's *K*-function for each 3D image or its part with MFDs are shown as indicated. All panels "a" show histograms for the entire 3D image containing both planes and for each plane separately (bottom traces). All panels "b" display the differential histograms, where histograms for both planes alone were subtracted from the histogram of the entire 3D image. The resulting differential histograms reflect the net inter-distances between the two modeled planes.

Supplementary data to this article can be found online at https://doi.org/10.1016/j.bbabio.2019.06.015.

Transparency document

The Transparency document associated with this article can be found, in online version.

Funding

This work was supported by the Grant Agency of the Czech Republic (Grantová Agentura České Republiky) [grant numbers 16-04788S and 17-08565S].

Author contributions

Andrea Dlasková: Conceptualization, Methodology, Validation,

Investigation, Visualization, Funding Acquisition. **Tomáš Špaček**: Conceptualization, Methodology, Validation, Formal Analysis, Investigation, Visualization. **Hana Engstová**: Conceptualization, Methodology, Validation, Formal Analysis, Investigation, Data Curation, Visualization. **Jitka Špačková**: Methodology, Resources, Investigation. **Adam Schröfel**: Methodology. **Blanka Holendová**: Methodology, Visualization. **Katarína Smolková**: Methodology, Resources, Investigation. **Lydie Plecitá-Hlavatá**: Conceptualization, Methodology, Investigation. **Petr Ježek**: Conceptualization, Methodology, Validation, Formal Analysis, Data Curation, Writing – Original Draft, Writing – Review & Editing, Visualization, Supervision, Project Administration, Funding Acquisition.

Acknowledgements

We gratefully acknowledge the help of Dr. Lukáš Alán with double 3D super-resolution imaging and the excellent technical assistance of Jana Vaicová with BN-PAGE and immunoblotting. We gratefully acknowledge the Imaging Methods core facility at BIOCEV, an institution supported by the MEYS CR (LM2015062 Czech-BioImaging), for their support with obtaining the FIB/SEM data presented in this paper.

References

[1] L. Plecitá-Hlavatá, H. Engstová, L. Alán, T. Špaček, A. Dlasková, K. Smolková, J. Špačková, J. Tauber, V. Strádalová, J. Malínský, M. Lessard, J. Bewersdorf, P. Ježek, Hypoxic HepG2 cell adaptation decreases ATP synthase dimers and ATP production in inflated cristae by mitofilin down-regulation concomitant to MICOS clustering, FASEB J. 30 (2016) 1941–1957.
[2] L. Plecitá, P. Ježek, Integration of superoxide formation and cristae morphology for mitochondrial redox signaling, Int. J. Biochem. Cell Biol. 80 (2016) 31–50.
[3] R. Quintana-Cabrera, A. Mehrotra, G. Rigoni, M.E. Soriano, Who and how in the regulation of mitochondrial cristae shape and function, Biochem. Biophys. Res. Commun. 500 (2018) 94–101.
[4] J. Nielsen, K.D. Gejl, M. Hey-Mogensen, H.C. Holmberg, C. Suetta, P. Krustrup, C.P.H. Elemans, N. Ørtenblad, Plasticity in mitochondrial cristae density allows metabolic capacity modulation in human skeletal muscle, J. Physiol. 595 (2017) 2839–2847.
[5] D.A. Patten, J. Wong, M. Khacho, V. Soubannier, R.J. Mailloux, K. Pilon-Larose, J.G. MacLaurin, D.S. Park, H.M. McBride, L. Trinkle-Mulcahy, et al., OPA1-dependent cristae modulation is essential for cellular adaptation to metabolic demand, EMBO J. 33 (2014) 2676–2691.
[6] C. Kukat, K.M. Davies, C.A. Wurm, H. Spåhr, N.A. Bonekamp, I. Kühl, F. Joos, P.L. Polosa, C.B. Park, V. Posse, M. Falkenberg, S. Jakobs, W. Kühlbrandt, N.G. Larsson, Cross-strand binding of TFAM to a single mtDNA molecule forms the mitochondrial nucleoid, Proc. Natl. Acad. Sci. U. S. A. 112 (2015) 11288–11293.
[7] L. Pernas, L. Scorrano, Mito-morphosis: mitochondrial fusion, fission, and cristae remodeling as key mediators of cellular function, Annu. Rev. Physiol. 78 (2016) 505–531.
[8] M. Harner, C. Körner, D. Walther, D. Mokranjac, J. Kaesmacher, U. Welsch, J. Griffith, M. Mann, F. Reggiori, W. Neupert, The mitochondrial contact site complex, a determinant of mitochondrial architecture, EMBO J. 30 (2011) 4356–4370.
[9] R.M. Zerbes, M. Bohnert, D.A. Stroud, K. von der Malsburg, A. Kram, S. Oeljeklaus, B. Warscheid, T. Becker, N. Wiedemann, M. Veenhuis, I.J. van der Klei, N. Pfanner, M. van der Laan, Role of MINOS in mitochondrial membrane architecture: cristae morphology and outer membrane interactions differentially depend on mitofilin domains, J. Mol. Biol. 422 (2012) 183–191.
[10] M. Bohnert, L.S. Wenz, R.M. Zerbes, S.E. Horvath, D.A. Stroud, K. von der Malsburg, J.M. Müller, S. Oeljeklaus, I. Perschil, B. Warscheid, A. Chacinska, M. Veenhuis, I.J. van der Klei, G. Daum, N. Wiedemann, T. Becker, N. Pfanner, M. van der Laan, Role of mitochondrial inner membrane organizing system in protein biogenesis of the mitochondrial outer membrane, Mol. Biol. Cell 23 (2012) 3948–3956.
[11] D.C. Jans, C.A. Wurm, D. Riedel, D. Wenzel, F. Stagge, M. Deckers, P. Rehling, S. Jakobs, STED super-resolution microscopy reveals an array of MINOS clusters along human mitochondria, Proc. Natl. Acad. Sci. U. S. A. 110 (2013) 8936–8941.
[12] M. Hessenberger, R.M. Zerbes, H. Rampelt, S. Kunz, A.H. Xavier, B. Purfürst, H. Lilie, N. Pfanner, M. van der Laan, O. Daumke, Regulated membrane remodeling by Mic60 controls formation of mitochondrial crista junctions, Nat. Commun. 8 (2017 May 31) 15258.
[13] C. Körner, M. Barrera, J. Dukanovic, K. Eydt, M. Harner, R. Rabl, F. Vogel, D. Rapaport, W. Neupert, A.S. Reichert, The C-terminal domain of Fcj1 is required for formation of crista junctions and interacts with the TOB/SAM complex in mitochondria, Mol. Biol. Cell 23 (2012) 2143–2155.
[14] S.W. Lackey, J.G. Wideman, E.K. Kennedy, N.E. Go, F.E. Nargang, The Neurospora crassa TOB complex: analysis of the topology and function of Tob38 and Tob37, PLoS One 6 (2011) e25650.
[15] N. Pfanner, M. van der Laan, P. Amati, R.A. Capaldi, A.A. Caudy, A. Chacinska, M. Darshi, M. Deckers, S. Hoppins, T. Icho, S. Jakobs, J. Ji, V. Kozjak-Pavlovic, C. Meisinger, P.R. Odgren, S.K. Park, P. Rehling, A.S. Reichert, M.S. Sheikh, S.S. Taylor, N. Tsuchida, A.M. van der Bliek, I.J. van der Klei, J.S. Weissman, B. Westermann, J. Zha, W. Neupert, J. Nunnari, Uniform nomenclature for the mitochondrial contact site and cristae organizing systém, J. Cell Biol. 204 (2014) 1083–1086.
[16] M. Barbot, D.C. Jans, C. Schulz, N. Denkert, B. Kroppen, M. Hoppert, S. Jakobs, M. Meinecke, Mic10 oligomerizes to bend mitochondrial inner membranes at cristae junctions, Cell Metab. 21 (2015) 756–763.
[17] M. Bohnert, R.M. Zerbes, K.M. Davies, A.W. Mühleip, H. Rampelt, S.E. Horvath, T. Boenke, A. Kram, I. Perschil, M. Veenhuis, W. Kühlbrandt, I.J. van der Klei, N. Pfanner, M. van der Laan, Central role of Mic10 in the mitochondrial contact site and cristae organizing system, Cell Metab. 21 (2015) 747–755.
[18] L. Scorrano, M. Ashiya, K. Buttle, S. Weiler, S.A. Oakes, C.A. Mannella, S.J. Korsmeyer, A distinct pathway remodels mitochondrial cristae and mobilizes cytochrome c during apoptosis, Dev. Cell 2 (2002) 55–67.
[19] C. Frezza, S. Cipolat, O. Martins de Brito, M. Micaroni, G.V. Beznoussenko, T. Rudka, D. Bartoli, R.S. Polishuck, N.N. Danial, B. De Strooper, L. Scorrano, OPA1 controls apoptotic cristae remodeling independently from mitochondrial fusion, Cell 126 (2006) 177–189.
[20] S. Cipolat, T. Rudka, D. Hartmann, V. Costa, L. Serneels, K. Craessaerts, K. Metzger, C. Frezza, W. Annaert, L. D'Adamio, C. Derks, T. Dejaegere, L. Pellegrini, R. D'Hooge, L. Scorrano, B. De Strooper, Mitochondrial rhomboid PARL regulates cytochrome c release during apoptosis via OPA1-dependent cristae remodeling, Cell 126 (2006) 163–175.
[21] S. Cogliati, C. Frezza, M.E. Soriano, T. Varanita, R. Quintana-Cabrera, M. Corrado, S. Cipolat, V. Costa, A. Casarin, L.C. Gomes, E. Perales-Clemente, L. Salviati, P. Fernandez-Silva, J.A. Enriquez, L. Scorrano, Mitochondrial cristae shape determines respiratory chain supercomplexes assembly and respiratory efficiency, Cell 155 (2013) 160–171.
[22] G. Civiletto, T. Varanita, R. Cerutti, T. Gorletta, S. Barbaro, S. Marchet, C. Lamperti, C. Viscomi, L. Scorrano, M. Zeviani, Opa1 overexpression ameliorates the phenotype of two mitochondrial disease mouse models, Cell Metab. 21 (2015) 845–854.
[23] W. Kühlbrandt, Structure and function of mitochondrial membrane protein complexes, BMC Biol. 13 (2015) 89.
[24] K.M. Davies, C. Anselmi, I. Wittig, J.D. Faraldo-Gomez, W. Kühlbrandt, Structure of the yeast F1Fo-ATP synthase dimer and its role in shaping the mitochondrial cristae, Proc. Natl. Acad. Sci. U. S. A. 109 (2012) 13602–13607.
[25] B. Daum, A. Walter, A. Horst, H.D. Osiewacz, W. Kühlbrandt, Age-dependent dissociation of ATP synthase dimers and loss of inner-membrane cristae in mitochondria, Proc. Natl. Acad. Sci. U. S. A. 110 (2013) 15301–15306.
[26] K.M. Davies, M. Strauss, B. Daum, J.H. Kief, H.D. Osiewacz, A. Rycovska, V. Zickermann, W. Kühlbrandt, Macromolecular organization of ATP synthase and complex I in whole mitochondria, Proc. Natl. Acad. Sci. U. S. A. 108 (2011) 14121–14126.
[27] M. Strauss, G. Hofhaus, R.R. Schröder, W. Kühlbrandt, Dimer ribbons of ATP synthase shape the inner mitochondrial membrane, EMBO J. 27 (2008) 1154–1160.
[28] C. Jiko, K.M. Davies, K. Shinzawa-Itoh, K. Tani, S. Maeda, D.J. Mills, T. Tsukihara, Y. Fujiyoshi, W. Kühlbrandt, C. Gerle, Bovine F1Fo ATP synthase monomers bend the lipid bilayer in 2D membrane crystals, Elife. (4) (2015) e06119.
[29] J. He, H.C. Ford, J. Carroll, C. Douglas, E. Gonzales, S. Ding, I.M. Fearnley, J.E. Walker, Assembly of the membrane domain of ATP synthase in human mitochondria, Proc. Natl. Acad. Sci. U. S. A. 115 (2018) 2988–2993.
[30] H. Kontro, J.J. Hulmi, P. Rahkila, H. Kainulainen, Cellular and tissue expression of DAPIT, a phylogenetically conserved peptide, Eur. J. Histochem. 56 (2012) e18.
[31] H. Kontro, G. Cannino, P. Rustin, E. Dufour, H. Kainulainen, DAPIT over-expression modulates glucose metabolism and cell behaviour in HEK293T cells, PLoS One 10 (2015) e0131990.
[32] S. Ohsakaya, M. Fujikawa, T. Hisabori, M. Yoshida, Knockdown of DAPIT (diabetes-associated protein in insulin-sensitive tissue) results in loss of ATP synthase in mitochondria, J. Biol. Chem. 286 (2011) 20292–20296.
[33] H. Päivärinne, H. Kainulainen, DAPIT, a novel protein down-regulated in insulin-sensitive tissues in streptozotocin-induced diabetes, Acta Diabetol. 38 (2001) 83–86.
[34] Y. Nagata, M. Yamagishi, T. Konno, C. Nakanishi, Y. Asano, S. Ito, Y. Nakajima, O. Seguchi, N. Fujino, M.A. Kawashiri, S. Takashima, M. Kitakaze, K. Hayashi, Heat failure phenotypes induced by knockdown of DAPIT in zebrafish: a new insight into mechanism of dilated cardiomyopathy, Sci. Rep. 7 (2017) 17417.
[35] M. Barbot, D.C. Jans, C. Schulz, N. Denkert, B. Kroppen, M. Hoppert, S. Jakobs, M. Meinecke, Mic10 oligomerizes to bend mitochondrial inner membranes at cristae junctions, Cell Metab. 21 (2015) 756–763.
[36] K. Eydt, K.M. Davies, C. Behrendt, I. Wittig, A.S. Reichert, Cristae architecture is determined by an interplay of the MICOS complex and the F1FO ATP synthase via Mic27 and Mic10, Microb Cell. 4 (2017) 259–272.
[37] H. Rampelt, M. Bohnert, R.M. Zerbes, S.E. Horvath, B. Warscheid, N. Pfanner, M. van der Laan, Mic10, a core subunit of the mitochondrial contact site and cristae organizing system, interacts with the dimeric F1Fo-ATP synthase, J. Mol. Biol. 429 (2017) 1162–1170.
[38] D. Fallaize, L.S. Chin, L. Li, Differential submitochondrial localization of PINK1 as a molecular switch for mediating distinct mitochondrial signaling pathways, Cell Sign. 27 (2015) 2543–2554.
[39] M. Wasilewski, M. Semenzato, S.M. Rafelski, J. Robbins, A.I. Bakardjiev, L. Scorrano, Optic atrophy 1-dependent mitochondrial remodeling controls steroidogenesis in trophoblasts, Curr. Biol. 22 (2012) 1228–1234.
[40] R. Schmidt, C.A. Wurm, A. Punge, A. Egner, S. Jakobs, S.W. Hell, Mitochondrial cristae revealed with focused light, Nano Lett. 9 (2009) 2508–2510.

[41] S.J. Sahl, S.W. Hell, S. Jakobs, Fluorescence nanoscopy in cell biology, Nat. Rev. Mol. Cell Biol. 18 (11) (2017) 685–701.
[42] M.J. Mlodzianoski, J.M. Schreiner, S.P. Callahan, K. Smolková, A. Dlasková, J. Šantorová, P. Ježek, J. Bewersdorf Sample drift correction in 3D fluorescence photoactivation localization microscopy, Opt. Express 19 (2011) 15009–15019.
[43] A. Dlasková, H. Engstová, T. Špaček, A. Kahancová, V. Pavluch, K. Smolková, J. Špačková, M. Bartoš, L. Plecitá-Hlavatá, P. Ježek, 3D super-resolution microscopy reflects mitochondrial cristae alternations and mtDNA nucleoid size and distribution, Biochim. Biophys. Acta 1859 (2018) 829–844.
[44] L. Plecitá-Hlavatá, J. Ježek, P. Ježek, Aglycemia keeps mitochondrial oxidative phosphorylation under hypoxic conditions in HepG2 cells, J. Bioenerg. Biomembr. 47 (2015) 467–476.
[45] L. Plecitá-Hlavatá, J. Ježek, P. Ježek, Aglycemic HepG2 cells switch from aminotransferase glutaminolytic pathway of pyruvate utilization to complete Krebs cycle at hypoxia, Front. Endocrinol. 9 (2018) 637.
[46] K. Smolková, L. Plecitá-Hlavatá, N. Bellance, G. Benard, R. Rossignol, P. Ježek, Waves of gene regulation suppress and then restore oxidative phosphorylation in cancer cells, Int. J. Biochem. Cell Biol. 43 (2011) 950–968.
[47] P. Ježek, L. Plecitá-Hlavatá, K. Smolková, R. Rossignol, Distinctions and similarities of cell bioenergetics and role of mitochondria in hypoxia, cancer, and embryonic development, Int. J. Biochem. Cell Biol. 42 (2010) 604–622.
[48] Z. Polianskyte, N. Peitsaro, A. Dapkunas, J. Liobikas, R. Soliymani, M. Lalowski, O. Speer, J. Seitsonen, S. Butcher, G.M. Cereghetti, M.D. Linder, M. Merckel, J. Thompson, O. Eriksson, LACTB is a filament-forming protein localized in mitochondria, Proc. Natl. Acad. Sci. U. S. A. 106 (2009) 18960–18965.
[49] M.O. Smith, J. Ball, B.B. Holloway, F. Erdelyi, G. Szabo, E. Stone, J. Graham, J.J. Lawrence, Measuring aggregation of events about a mass using spatial point pattern methods, Spat Stat. 13 (2015) 76–89.
[50] P.R. Nicovich, D.M. Owen, K. Gaus, Turning single-molecule localization microscopy into a quantitative bioanalytical tool, Nat. Protocols 12 (3) (2017) 453–461.
[51] D.M. Owen, D.J. Williamson, L. Boelen, A. Magenau, J. Rossy, K. Gaus, Quantitative analysis of three-dimensional fluorescence localization microscopy data, Biophys. J. 105 (2) (2013) L05–L07.
[52] M.C. Willingham, A.V. Rutherford, The use of osmium-thiocarbohydrazide-osmium (OTO) and ferrocyanide-reduced osmium methods to enhance membrane contrast and preservation in cultured cells, J. Histochem. Cytochem. 32 (4) (1984) 455–460.
[53] F. Baumgart, A.M. Arnold, K. Leskovar, K. Staszek, M. Folser, J. Weghuber, H. Stockinger, G.J. Schutz, Varying label density allows artifact-free analysis of membrane-protein nanoclusters, Nat. Methods 13 (2016) 661–664.
[54] J. Sjöholm, J. Bergstrand, T. Nilsson, R. Šachl, C.V. Ballmoos, J. Widengren, P. Brzezinski, The lateral distance between a proton pump and ATP synthase determines the ATP-synthesis rate, Sci. Rep. 7 (2017) 2926.
[55] C. Anselmi, K.M. Davies, J.D. Faraldo-Gómez, Mitochondrial ATP synthase dimers spontaneously associate due to a long-range membrane-induced force, J. Gen. Physiol. 150 (2018) 763–770.
[56] M.E. Harner, A.K. Unger, W.J. Geerts, M. Mar, T. Izawa, M. Stenger, S. Geimer, F. Reggiori, B. Westermann, W. Neupert, An evidence based hypothesis on the existence of two pathways of mitochondrial crista formation, Elife 5 (2016) e18853.
[57] E. Bisetto, M. Comelli, A.M. Salzano, P. Picotti, A. Scaloni, G. Lippe, I. Mavelli, Proteomic analysis of F1F0-ATP synthase super-assembly in mitochondria of cardiomyoblasts undergoing differentiation to the cardiac lineage, Biochim. Biophys. Acta 1827 (2013) 807–816.
[58] H. Guo, S. Bueler, J.L. Rubinstein, Atomic model for the dimeric FO region of mitochondrial ATP synthase, Science 358 (2017) 936–940.
[59] N. Klusch, B.J. Murphy, D.J. Mills, Ö. Yildiz, W. Kühlbrandt, Structural basis of proton translocation and force generation in mitochondrial ATP synthase, Elife 6 (2017) e33274.
[60] R. Quintana-Cabrera, C. Quirin, C. Glytsou, M. Corrado, A. Urbani, A. Pellattiero, E. Calvo, J. Vázquez, J.A. Enríquez, C. Gerle, M.E. Soriano, P. Bernardi, L. Scorrano, The cristae modulator Optic atrophy 1 requires mitochondrial ATP synthase oligomers to safeguard mitochondrial function, Nat. Commun. 9 (2018) 3399.